UNIVERSIDAD DE ANTIOQUIA

Facultad de Ciencias Exactas y Naturales

MASTER THESIS IN PHYSICS

Scalar potential analysis of the $\mathbb{Z}_5$ multi-component dark matter model

MASTER CANDIDATE

Diego Alejandro Ríos Pérez

SUPERVISOR

PhD Oscar A. Zapata

Universidad de Antioquia

MEDELLÍN, COLOMBIA

ACADEMIC YEAR
2023

*To my parents, friends,
and especially to my wife Evelyn.*

Abstract

In recent years the multi-component scalar dark matter models with discrete symmetries $\mathbb{Z}_N$ have been widely studied in the literature. Among them, the $\mathbb{Z}_5$ model proposes two complex fields that transform as singlets under the Standard Model gauge group. The scalar potential brings along with eleven free parameters that must be restricted. In that sense, the primary purpose of this research is to develop a detailed analysis of the scalar potential with the objective of establishing the perturbative unitarity, vacuum stability, and positivity conditions, and finally to determine the viable parameter space of the model.

Resumen

En los últimos años, los modelos de materia oscura escalar multicomponente con simetrías discretas $\mathbb{Z}_N$ han sido ampliamente estudiados en la literatura. Entre ellos, el modelo $\mathbb{Z}_5$ propone dos campos complejos que transforman como singletes bajo el grupo de gauge del modelo estándar. El potencial escalar trae consigo once parámetros libres que deben ser restringidos. En ese sentido, el propósito principal de esta investigación es desarrollar un análisis detallado del potencial escalar con el objetivo de establecer las condiciones de unitaridad perturbativa, estabilidad del vacío, estabilidad del potencial, positividad, y finalmente determinar el espacio de parámetros viable del modelo.

Contents

List of Figures

List of Tables

List of Acronyms

BBN Big Bang Nucleosyntesis

CMB Cosmic Microwave Background

COBE Cosmic Background Explorer

DM Dark Matter

DMR Differential Microwave Radiometer

FRW Friedmann-Robertson-Waker

GUTs Grand Unification Theories

LHC Large Hadron Collider

LZ LUX-ZEPLIN

PandaX Particle and Astrophysical Xenon Detector

RGEs Renormalization Group Equation

SM Standard Model

WIMPs Weakly Interacting Massive Particles

WMAP Wilkinson Microwave Anisotropy Probe

1

Introduction

One of the great hit of physics in the past century is the Standard Model (SM) of the particle physics, which explains a part of the observable universe through a set of seventeen particles. The SM is then a well-structured quantum field theory that describes the electroweak and strong interactions under the assumption that these follow the transformation rules of the $U(1)_Y \otimes SU(2)_L \otimes SU(3)_c$ symmetry group. However, in the first half of the last century some anomalies were observed in different situations where the SM and general relativity would have explained the phenomena but they do not do it correctly, for instance, the expected rotation speed of some galaxies in distant clusters, the characteristic angle of gravitational lensing due to a galaxy, the homogeneity of the radiation in the photon decoupling epoch, etc [1–9]. The inconsistency is in the fact that the baryonic matter is not sufficient to explain some observed cosmological phenomena; therefore, due to the non-observable features of the missing matter

that complete the phenomena explanations, this was called Dark Matter (DM).

The ordinary (baryonic) matter only composes roughly 5% of the total mass-energy density in the current cosmological paradigm (ΛCDM), whilst the DM constitutes about 27% and the rest is given by dark energy [10]. This means that dark (baryonic) matter represents about 84% (16%) of the total matter in the universe. Though the abundance of DM is higher than the baryonic matter, this has been detected only through its gravitational interactions. Thus, in recent years several theories and models have surged in order to explain this kind of matter and how it works [11–13].

In the rest of this chapter, we discuss some of the early evidence supporting the existence of DM in the section 1.1 while in 1.2 modern evidence. The so-called Weakly Interacting Massive Particles (WIMPs) paradigm in section 1.3, and finally the introduction of models with scalar dark matter stabilized by $\mathbb{Z}_N$ symmetries in section 1.4.

1.1 EARLY EVIDENCE

Usually, in the literature, the first event where the first dark matter effects were detected is attributed to the Coma Cluster's studies developed by Zwicky in his paper published in 1937 [4]. The Coma Cluster is about 99 Mpc from Earth and using the method of Doppler shifts analysis in the galactic spectra, Zwicky calculated the velocity dispersion of the galaxies in this cluster. According to Newton's theory, the relationship between gravitational and centripetal strength

leads to the relation

$$m\frac{[v(r)]^2}{r} = G\frac{mM(r)}{r^2} \tag{1.1}$$

outside the region where the majority of galaxy mass is enclosed. Therefore, the rotation velocity of the object at a radius r is given by $v(r) = \sqrt{GM(r)/r}$, being $M(r)$ the mass contained in the region within r, and G the usual gravitational constant. There exist a "Keplerian" behavior $v(r) \propto 1/\sqrt{r}$, which suggests that the rotation velocity must decrease according to the inverse of the square root of the radius.

Around the same time, as Zwicky made his discovery, Oort [2] found that the motion of stars in the Milky Way is so fast that their velocities should allow them to escape the gravitational pull of the luminous mass in the galaxy. One of the lights from the galactic center is not visible by dust or other bodies which obscured its track to the Earth, therefore the Doppler shifts can not be totally described.

Zwicky unlike Oort calculated the specific missing mass that could cause these behaviors. Following the virial theorem, giving the relation between the average kinetic and potential energy in the Coma cluster $\langle U \rangle = -2\langle T \rangle$, Zwicky found that the mass in the cluster is roughly $4.5 \times 10^{13} M_\odot$.

On the other hand, the mass of the ~ 1000 nebulae in the cluster in around $4.5 \times 10^{10} M_\odot$, a result that is not consistent since the measurement through the usual standard ratio between the mass of the nebulae and its luminosity (M/L), gave a total mass of approximately 2% of this value [14, 15]. Then, the majority

of the mass in the Coma cluster is not visible for some reason (non-luminous).

After roughly 40 years following the above discoveries, in the 1970's, Vera Rubin and collaborators [16] performed a more detailed study of the rotational velocities in spiral galaxies, specifically 60 isolated galaxies were chosen for calculating the relations between the distance of the center and the rotational velocity. They employed the analysis of spectral lines such that the material on one side of the galactic nucleus was approaching our galaxy and on the other side was receding. This analysis gave also angular information about the distance of the target object in the galaxy from the center. As above, in the Zwicky studies, Vera Rubin found a contradiction with the keplerian behavior $v(r) \propto 1/\sqrt{r}$. According to Gauss's law for the gravitational field, one expects that one gaussian surface which encloses a gravitational mass $M(r)$, will have a flux

$$M(r) = (1/4\pi G) \int_S \vec{g} \cdot d\vec{A}, \tag{1.2}$$

then $\vec{g}$ increases if $M(r)$ increases with r, but $\vec{g}$ decreases if this mass enclosed decreases or remains constant while r increases; thus $\vec{g}$ will fall giving smaller $v(r)$ ar large r. Since at some r the density of luminous mass falls but the stars acquire high velocities, the important conclusion is that the missing mass is not luminous and is not concentrated near the center of spiral galaxies. The figure 1.1 shows the measurement developed by Vera Rubin for rotational velocities.

In the same decade, was observed another event that probes the presence of DM in the cosmological context. In Einstein's theory of relativity, there is an
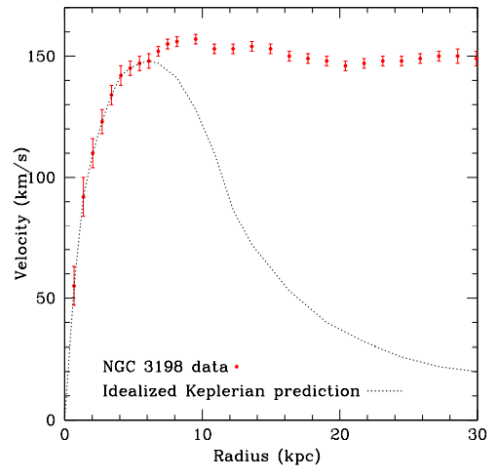
Figure 1.1: Measurement of the rotation velocities for stars into the NGC 3198 barred spiral galaxy. The red dots represent the experimental data taken by Vera Rubin and collaborators and the dotted line is the predicted (kepplerian) behavior [14].

interesting effect associated with the curvature of the light around a massive object like a cluster of galaxies, called *gravitational lensing* [17, 18]. If there is a galaxy located directly behind the cluster of galaxies, we may observe an "Einstein ring" around this massive object. The likelihood of two appropriate objects lining up perfectly with the Earth is low, but in 1979, Walsh *et* al. [7], were the first to observe this. Figure 1.2 shows the observed gravitational lensing called LRG 3-757 Cosmic Horseshoe. For a calculation of "Einstein radius" (the radius of an arcle in radians), associated with the "amount" of gravitational lensing effect [14], Einstein's theory leads to

$$\theta_E \propto M_{\text{cluster}}. \tag{1.3}$$

5

Figure 1.2: The LRG 3-757 Cosmic Horseshoe. It is a gravitational lens to 11 billion light years away.

The studies show that the mass calculated through this theory is much larger than the mass obtained by implementing the usual ratio of mass-luminosity M/L.

1.2   MODERN COSMOLOGICAL EVIDENCE

The general theory of standard cosmology so-called the Friedmann-Robertson-Waker (FRW) cosmological model or the Hot Big Bang model is so successful and allows us to understand the total evolution of the universe [19]. The FRW cosmology is so robust that it is possible to make sensible speculations about the universe at times as early as 10^{-3} seconds after the bang. The theory then may explain the Big Bang Nucleosyntesis (BBN), where the universe had a few seconds of age. The deuterium, helium, lithium, and other light elements were the first in be formed at the BBN . All the sources of deuterium come from the BBN epoch and when it is produced into stars or other sites, this immediately is destroyed by fusing it into ^{4}He. Therefore, the abundance of this element is a

key piece since the current abundance must be a lower limit of the initial amount created at the BBN epoch [14,20].

Using nuclear physics and the ratio between the observable deuterium abundance and the hydrogen abundance, we are able to calculate BBN elemental abundances. In fact, the FRW cosmological model has the important triumph of the precise agreement between the observable abundance and the theoretical predictions for several elements. The ratio between deuterium and hydrogen leads to the numerical density of baryons in the universe, giving $\Omega_b h^2$, where Ω_b is the baryon density relative to a reference critical density ρ_c, and $h = H/100$ $\mathrm{km\,s}^{-1}\,\mathrm{Mpc}^{-1}$ is the reduced Hubble constant.

The Cosmic Microwave Background (CMB) was discovered by Penzias and Wilson in 1965 as an excess background temperature of about 2.73 K [9]. It is a remnant from the epoch when the universe was $380\,000$ years old, therefore analyzing it we can obtain information about the composition of the early universe. In this epoch, the free protons and electrons of the primordial plasma form the neutrally charged atoms. The CMB is then the last scattering surface from the early universe.

The CMB is a nearly perfect blackbody, hence we can use statistical thermodynamics to describe the early universe. However, the Differential Microwave Radiometer (DMR) of Cosmic Background Explorer (COBE) showed in 1989, that CMB has fundamental anisotropies (fluctuations) of only about $30 \pm 5\ \mu\mathrm{K}$ [21]. The figure 1.3 shows the CMB fluctuations and their representation through

spherical harmonics.
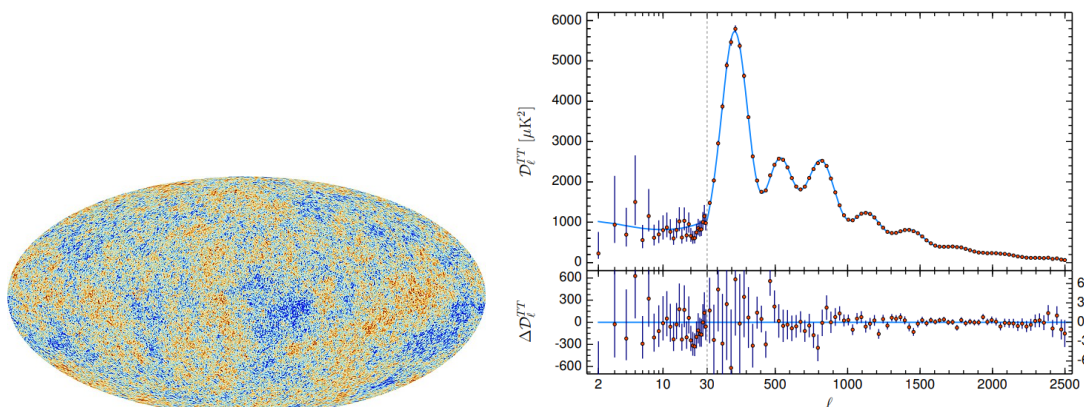
Figure 1.3: The CMB fluctuations (left), and the power spectrum of the fluctuations as a function of the angular moment (right) [10].

A possible explanation for these fluctuations (at large scales) may be since at the time of the last scattering there were areas with larger density and thus, lower photons are observed today. Another explanation (at small scales) is due to *acoustic oscillations*: before photons decoupling, the fluid of protons-photons is compressed by the gravitational well; the pressure of the fluid in this process increases but after decreases since it expands outward due to the high pressure; finally, the gravity pulls it back and the cycle repeats so that we understand this as an oscillation into the plasma. The CMB fluctuations turn out then that in the early universe there was a gravitational dynamic in the proton-photon fluid.

The problem in the explanation of the universe is that considering only baryonic matter before photon decoupling in the fluid, the current structures could not be observed since, e.g. in the acoustic oscillations dynamics, the electrostatic forces do not allow to perform the cycle. In that epoch, protons and electrons had not been recombined, then all the ordinary matter was charged.

It suggests that there was an electrically neutral kind of matter which promoted the gravitational effects of forming structure.

The Wilkinson Microwave Anisotropy Probe (WMAP) was launched in 2001 to develop a precise measure of the anisotropies in the CMB [22]. With this collaboration, we start the knowledge of the total and baryonic matter densities. Currently, the latest results obtained from these parameters were presented by PLANCK collaboration in 2018 [10]. The total matter density and the baryonic matter density (relative to a critic matter density) are

$$\Omega_{\mathrm{M}}h^2 = 0.1430 \pm 0.0011, \quad \Omega_{\mathrm{BM}}h^2 = 0.02237 \pm 0.00015, \tag{1.4}$$

therefore baryonic matter is not the only form of matter in the universe.

The dark matter relic density is given by

$$\Omega_{\mathrm{DM}}h^2 = \left(\Omega_{\mathrm{M}} - \Omega_{\mathrm{BM}}\right)h^2 = 0.1200 \pm 0.0012, \tag{1.5}$$

which is roughly 83% of the total matter density.

1.3 THE WIMP PARADIGM

In recent years, many dark matter candidates have been proposed and one of the better motivated are the WIMPs [23,24] since they are electrically neutral and the theoretical considerations lead to appropriate number densities to compose

the DM in the current universe [25–27]. This term was coined by Gary Steigman and Michael Turner in 1984 [28], originally to include all particle dark matter candidates in the epoch.

The early universe was very hot, and massive and energetic particles were created. However, while the universe expanded it cooled, and the number of particles stabilized due to the interactions occurring with low frequency. In addition, the lighter particles lose kinetic energy to produce heavier particles through interactions; then lighter particles fill the majority of the universe. According to the above arguments, in the early universe the DM numeric density decreases but at some point, it stabilizes because of the low frequency of interactions with other particles. In that moment, the thermal equilibrium of the universe is violated, and the DM number density "freezes in". This final number density at the time of freeze-out is known as the *relic density* of DM. See e.g. [19] for a deep exposition of the topic.

In order to calculate the number density of a specific particle as DM, we may implement the Boltzmann equation which describes the temporal evolution of the numeric density for a particle specie taking into account the decay into other particles, the co-annihilations, scattering off of the thermal background and the expansion of the universe. The temporal evolution of the numeric density of a χ-DM particle which interacts with a X-SM particle reads

$$\frac{dn_\chi}{dt} = -\left\langle \sigma_{\chi\overline{\chi}\to X\overline{X}}|v| \right\rangle \left[n_\chi^2 - \left(n_X^{\text{EQ}} \right)^2 \right] - 3Hn_\chi \tag{1.6}$$

where $\left\langle \sigma_{\chi\bar{\chi}\to X\bar{X}}|v|\right\rangle$ is the thermally-averaged annihilation cross section, v the relative velocity of the particles in the thermal bath, n_X^{EQ} the equilibrium value of n_X, and H is the Hubble constant. However, as the model studied in this research, there are interaction terms that allow semi-annihilation processes in the early universe, and in the case of more than one DM particle ($\chi_1, \chi_2 \ldots \chi_N$), we would have conversion processes if they interact among themselves. For the temporal evolution of the DM particle χ_i, the Boltzmann equation can be written completely as

$$\frac{dn_{\chi_i}}{dt} = -\sum_{\substack{j,k,l=1, \\ k,l\neq i}}^{N} \left\{ \underbrace{\left\langle \sigma_{\chi_i\chi_j\to XX}|v|\right\rangle}_{\text{annihilations}} \left[n_{\chi_i}n_{\chi_j} - \left(n_X^{\text{EQ}}\right)^2 \right] \right.$$

$$+ \underbrace{\left\langle \sigma_{\chi_i\chi_j\to\chi_k X}|v|\right\rangle}_{\text{semi-annihilations}} \left(n_{\chi_i}n_{\chi_j} - n_{\chi_k}^{\text{EQ}}n_X^{\text{EQ}} \right)$$

$$\left. + \underbrace{\left\langle \sigma_{\chi_i\chi_j\to\chi_k\chi_l}|v|\right\rangle}_{\text{conversions}} \left(n_{\chi_i}n_{\chi_j} - n_{\chi_k}^{\text{EQ}}n_{\chi_l}^{\text{EQ}} \right) \right\} - 3Hn_{\chi_i}. \qquad (1.7)$$

Motivated by the WIMP paradigm, in recent years have been several experiments that are expected to detect any signal of this kind using the fact that it can interact directly with the baryonic matter: *direct* detection experiments. They consist on detecting WIMP scattering off of a nuclei of some element so sensitive to any energy change from the motion of the atoms within it, i.e., an element that allows reconstructing events of the type DM + SM → DM + SM, by analyzing the fluctuations on the energy of each zone of the element through a detector that contains it, and neglecting background events which seem like the target

event. We are assuming that the DM is traveling around every place in our local galaxy, then must exist a probability that it interacts with the observable baryonic matter. The amount of energy that a WIMP deposits in the target element is around $\sim$27 keV, considering that the DM moves at velocities of about 220 km/s with a mass of $\sim$100 GeV [14]. The radiation, in general deposits more energy of the MeV order, thus the detection of signals in the keV order are very difficult to reconstruct. Therefore, the experiments must ensure that the target element for the scattering with WIMPs be radioactively clean. Among the current experiments in the direct detection field, there are the LUX-ZEPLIN (LZ) experiment [29] at Sanford Underground Research Facility, the Particle and Astrophysical Xenon Detector (PandaX) [30] at China Jinping Underground Laboratory, and XENON experiment [31] at Italian Gran Sasso National Laboratory. All of them work with a tank with 3 to 10 tons of xenon which is a very sensitive material allowing the easy detection of energy depositions. In general, they constraint the spin-independent cross section for the scattering off of a WIMP with nuclei of xenon. There are many experiments, however, the aformentioned have imposed the most restricted bounds over this physical observable.

1.4 Scalar dark matter and multi-component scenarios with $\mathbb{Z}_N$ symmetries

The WIMPs are the most popular candidates and since the discovery of the Higgs boson by CMS [32] and ATLAS [33] experiments at the Large Hadron Collider (LHC), the scalar DM has taken a better position in the description of WIMPs. Hence the discrete $\mathbb{Z}_N$ symmetries which stabilize this kind of candidate are well motivated, furthermore, these models adjust to the results of recent collaborations and N-body simulations. The first of them to be proposed was the scalar singlet model [34], which contains a DM particle stabilized by a Z_2 symmetry,

$$\mathcal{L}_{\mathbb{Z}_2} = \frac{1}{2}(\partial\phi)^2 - \frac{1}{2}m_\phi^2\phi^2 - \frac{1}{4}\lambda\phi^2|H|^2, \tag{1.8}$$

where ϕ is the new real scalar field candidate to DM and H is the SM-like Higgs doublet. The main problem with this model is that recent results from direct and indirect detection experiments, have shown that the parameter space must be widely restricted in order to adjust the model with the predicted spin-independent cross-section for elastic scattering of ϕ with nuclei, according to direct detection experiments data [35]. On the other hand, the non-consistency of the model with N-body simulations, the DM density in galaxy centers and dwarf galaxies, and other cosmological observations suggest the DM freeze-out processes may be non-standard [36] including more complicated dynamics that

the $\mathbb{Z}_2$ does not allows such as semi-annihilations processes [37–39]. These kinds of interactions are viable in $\mathbb{Z}_N$ models with $N \geq 3$. Also, we may have a scenario of multi-component DM allowed by the other $\mathbb{Z}_N$ symmetries. Generically, this kind of model stabilizes the SM Higgs potential through interactions between scalar DM couplings with the Higgs boson which imply that the SM particles interact with DM via the so-called "Higgs portal"; then, instead of including new mediators in the dark sector to establish interactions between DM and SM particles as other models propose, the $\mathbb{Z}_N$ models allow interactions of the DM particles with the Higgs boson.

Motivated by the above problems and the recent results which restrict the WIMP paradigm, the $\mathbb{Z}_N$ models arise as an alternative of multi-component DM including non-standard processes, e.g. DM conversions and semi-annihilations. In general, the $\mathbb{Z}_N$ framework is viable by implementing abelian $\mathbb{Z}_N$ or discrete non-abelian symmetries [40,41], therefore there are many of possible scalar DM models. For a better exposition of this kind of model, see [42].

A $\mathbb{Z}_N$ symmetry can appear as a remnant from the spontaneous breaking of either a $U(1)_X$ gauge symmetry by a scalar field S with X charge equal to N or a $SU(N)$ gauge group by a scalar multiplet transforming as the adjoint representation, therefore we can relate the DM stability to gauge extensions of the SM such as Grand Unification Theories (GUTs).

The $\mathbb{Z}_N$ group is generated by the N Nth roots of 1 and consists of transfor-

mations of the form

$$\phi \rightarrow \omega_N^{X_\phi} \phi, \tag{1.9}$$

where ϕ is a scalar field and the $\omega_N^{X_\phi}$ factor is the charge of ϕ under the $\mathbb{Z}_N$ group. As an usual assumption [42], the SM particles are singlets under this symmetry and the new scalar particles are singlets under the gauge group of SM. Since $\omega_N^N = 1$ with $\omega_N = e^{i2\pi/N}$, we restrict the possible charge values to $\omega_N^{X_\phi} = 1, \omega, \omega_N^2, ..., \omega_N^{N-1}$ for $N \geq 3$ in order to stabilize the DM. In addition, for two or more fields, they must have different charges to avoid mixing among them and thus avoid that the lightest be the only stable field.

Given $(\omega_N^{X_\phi})^* = \omega_N^{-X_\phi} = \omega_N^{N-X_\phi}$, we observe that the maximum number of scalar fields charged under $\mathbb{Z}_N$ is $\lfloor N/2 \rfloor$. There are $k \leq \lfloor N/2 \rfloor$ scalar fields $\phi_{X_\phi} \sim \omega_N^{X_\phi}$ with X_ϕ different for each one. However, if N is odd, all the fields are complex, but if N is even, one of the fields must be real since necessarily it would have a charge equal to $\omega_N^{N/2} = -1$, then $\omega_N^{X_\phi} = \left(\omega_N^{X_\phi}\right)^* = -1$ and the field is real. For instance, the $\mathbb{Z}_4$ symmetry group is composed by the four 4th roots of 1, $\left\{1, e^{i\pi/2}, e^{i\pi}, e^{i3\pi/2}\right\}$ and with $N/2 = 2$, there are two possible scalar fields in the model; however, neglecting the trivial transformation in order to ensure stability, we can only choose the transformations $\phi_1 \rightarrow e^{i\pi/2}\phi_1$ and $\phi_2 \rightarrow -\phi_2$ due that $3 = -1 \mod 4$, then ϕ_2 is a real field. For a similar argument, the $\mathbb{Z}_3$ symmetry group only allows one complex scalar DM particle although the charges are $1, \omega_3$ and ω_3^2, we know that $2 = -1 \mod 3$; therefore $\phi \rightarrow e^{i2\pi/3}\phi$ is the only allowed transformation. The scenario with k DM particles may be minimally realized by

a $\mathbb{Z}_{2k}$ symmetry. In that sense, $\mathbb{Z}_4$ ($\mathbb{Z}_5$) is the lowest $\mathbb{Z}_N$ symmetry consistent with two-component DM (two-component of complex DM) composed by a complex scalar field ϕ_1 and a real scalar field ϕ_2 (composed by two complex scalar fields ϕ_1 and ϕ_2). $\mathbb{Z}_6$ ($\mathbb{Z}_7$) is the smallest $\mathbb{Z}_N$ symmetry that allows three DM particles (three complex DM particles), two of them complex scalar fields $\phi_{1,2}$ and one real scalar field ϕ_3 (all of them complex scalar fields $\phi_{1,2,3}$).

The DM stability is not only guaranteed by symmetry transformations. The DM particles can not acquire vacuum expectation value (vev) since this leads to $\mathbb{Z}_N$ symmetry breaking, therefore it must imposed that

$$\langle \phi_i \rangle_0 = 0, \tag{1.10}$$

such that the symmetry remains unbroken.

One must ensure that all the possible decays of ϕ_i into other ϕ_j's ($i \neq j$) are kinematically forbidden. This imposes restrictions on the masses of the scalar fields, for instance, in the case of $\mathbb{Z}_4$ model it includes the invariant terms $\phi_1^2 \phi_2 + \text{h.c.}$ where $\phi_1 \sim \omega_4$ and $\phi_2 \sim \omega_4^2$; there may be decays of the form $\phi_2 \rightarrow 2\phi_1$. To forbid this, the masses $M_{1,2}$ of the scalar fields $\phi_{1,2}$ (without loss of generality $M_1 < M_2$) must fulfill the relation $M_2 < 2M_1$ to avoid decays of one particle into the another particle.

In the following chapter (2), we will discuss the considerations and features of the case $N = 5$, which is the center of this research. In the chapter 3 we show the theoretical bounds that have to be imposed on the model in order to describe

a viable DM scenario. The chapter 4 exposes the result of implementing all of the constraints considered in the previous chapter. Finally, the work concludes with the chapter 5, where we discuss the obtained results and list some conclusions around them.

2

The $\mathbb{Z}_5$ model

The $\mathbb{Z}_5$ group contains the five 5th roots of 1,

$$\mathbb{Z}_5 = \{\omega_5^\alpha = \exp(i2\pi\alpha/5), \text{ with } \alpha = 0, 1, \ldots, 4\} . \tag{2.1}$$

Since $4 = -1 \mod 5$ and $3 = -2 \mod 5$, we are left with the charged ω_5 and ω_5^2. As was previously mentioned, the $\mathbb{Z}_5$ model is the lowest $\mathbb{Z}_N$ which allows a scenario of two-component of DM. The fields transform as

$$\phi_1 \sim \omega_5, \quad \phi_2 \sim \omega_5^2; \qquad \omega_5 = e^{i2\pi/5} . \tag{2.2}$$

Due to the different charges under $\mathbb{Z}_5$, as was exposed above, they do not mix and the quadratic terms in Lagrangian only include the fields as mass eigenstates.

The invariant interaction terms are

$$\mathcal{V}_2 \supset \phi_1\phi_1^*, \ \phi_2\phi_2^*; \tag{2.3}$$

$$\mathcal{V}_3 \supset \phi_1^2\phi_2^*, \ \phi_2^2\phi_1; \tag{2.4}$$

$$\mathcal{V}_4 \supset \phi_1^2\phi_1^{*2}, \ \phi_2^2\phi_2^{*2}, \ \phi_1\phi_1^*\phi_2\phi_2^*, \ \phi_1^3\phi_2, \ \phi_1\phi_2^{*3}. \tag{2.5}$$

The most general renormalizable scalar potential at tree level, invariant under $\mathbb{Z}_5$ symmetry reads

$$\mathcal{V} = -\mu_H^2|H|^2 + \lambda_H|H|^4 + \mu_1^2|\phi_1|^2 + \lambda_{S1}|H|^2|\phi_1|^2 + \lambda_{41}|\phi_1|^4 + \mu_2^2|\phi_2|^2$$

$$+ \lambda_{42}|\phi_2|^4 + \lambda_{S2}|H|^2|\phi_2|^2 + \lambda_{412}|\phi_1|^2|\phi_2|^2$$

$$+ \frac{1}{2}\left(\mu_{S1}\phi_1^2\phi_2^* + \mu_{S2}\phi_2^2\phi_1 + \lambda_{31}\phi_1^3\phi_2 + \lambda_{32}\phi_1\phi_2^{*3} + \text{h.c.}\right), \tag{2.6}$$

where H is the SM-like Higgs doublet. The scalar fields are singlets under the SM gauge group and the SM particles are singlets under the $\mathbb{Z}_5$ symmetry.

The new complex scalar fields do not acquire vev, so both are stable. Without loss of generality, we study the case $M_1 < M_2$. The terms $\phi_1^2\phi_2^*$ and $\phi_1^3\phi_2$ would lead to decays of the form $\phi_2^* \to 2\phi_1$ and $\phi_2 \to 3\phi_1$, then we must impose the condition $M_1 < M_2 < 2M_1$ to avoid decays of ϕ_2 into ϕ_1. Defining the Higgs doublet as $H = (G^+, (h + v_H)/\sqrt{2})^T$, where $v_H = 246$ GeV is the Higgs doublet vev, the Higgs mass term is obtained with $\partial\mathcal{V}/\partial h|_{\mathbf{\Phi}=0}$ where $\mathbf{\Phi} = (h, \phi_1, \phi_2)$,

$$-\mu_H^2 = \lambda_H v_H^2. \tag{2.7}$$

The mass-squared matrix is obtained by performing $\left(\boldsymbol{M}^2\right)_{ij} = \partial^2 \mathcal{V}/\partial\phi_i \partial\phi_j^* \big|_{\Phi=0}$, where $i, j = 0, 1, 2$ and $\phi_0 = h$. We have then

$$\boldsymbol{M}^2 = \begin{pmatrix} M_h^2 & 0 & 0 \\ 0 & M_1^2 & 0 \\ 0 & 0 & M_2^2 \end{pmatrix}, \tag{2.8}$$

where

$$M_h^2 = 2\lambda_H v_H^2, \tag{2.9}$$

$$M_1^2 = \mu_1^2 + \frac{1}{2}\lambda_{S1} v_H^2, \tag{2.10}$$

$$M_2^2 = \mu_1^2 + \frac{1}{2}\lambda_{S1} v_H^2. \tag{2.11}$$

Fixing the value of the Higgs self-coupling as $\lambda_H = 0.129$, the parameter space is reduced of thirteen to eleven free parameters: seven dimensionless (λ_{4i}, λ_{Si}, λ_{412} and λ_{3i}) and four dimensionful (M_i and μ_{Si}). after the spontaneous symmetry breaking, the full scalar potential can be written as

$$\begin{aligned} \mathcal{V} = {} & \frac{1}{2}M_h^2 h^2 + \lambda_H v_H h^3 + \frac{1}{4}\lambda_H h^4 \\ & + \sum_{i=1}^{2} \left(M_i^2 |\phi_i|^2 + \lambda_{4i}|\phi_i|^4 + \lambda_{Si} v_H h |\phi_i|^2 + \frac{1}{2}\lambda_{Si} h^2 |\phi_i|^2 \right) + \lambda_{412}|\phi_1|^2|\phi_2|^2 \\ & + \frac{1}{2}\left(\mu_{S1}\phi_1^2\phi_2^* + \mu_{S2}\phi_2^2\phi_1 + \lambda_{31}\phi_1^3\phi_2 + \lambda_{32}\phi_1\phi_2^{*3} + \text{h.c.} \right) \end{aligned} \tag{2.12}$$

The main characteristic of the model resides in the terms

$$\mathcal{V} \supset \mu_{S1}\phi_1^2\phi_2^* + \mu_{S2}\phi_1\phi_2^2 + \lambda_{31}\phi_1^3\phi_2 + \lambda_{32}\phi_1\phi_2^{*3} + \text{h.c.,} \qquad (2.13)$$

allowed by the new symmetry. Whilst models invariant under other $\mathbb{Z}_N$ symmetries as the $\mathbb{Z}_3$ model, only allow a new DM semi-annihilation term, this model has a set of new processes associated with DM conversion and semi-annihilation. Therefore, we have relevant terms that may change the number density of DM in the early universe.

In the table 2.1, are listed all the processes which modify the relic abundance of each DM particle according to the terms in the $\mathbb{Z}_5$ scalar potential [43].

ϕ_1 processes	Type	ϕ_2 processes	Type
$\phi_1 + \phi_1^* \to h + h$	1100	$\phi_2 + \phi_2^* \to h + h$	2200
$\phi_1 + \phi_1^* \to \phi_2 + \phi_2^*$	1122	$\phi_2 + \phi_2^* \to \phi_1 + \phi_1^*$	2211
$\phi_1 + h \to \phi_2 + \phi_2$	1022	$\phi_2 + \phi_2 \to \phi_1^* + h$	2210
$\phi_1 + \phi_2^* \to \phi_2^* + \phi_2^*$	1222	$\phi_2 + \phi_2 \to \phi_1 + \phi_2^*$	2212
$\phi_1 + \phi_1 \to \phi_1 + \phi_2$	1112	$\phi_2 + \phi_1 \to \phi_1^* + \phi_1^*$	2111
$\phi_1 + \phi_2 \to \phi_2 + h$	1220	$\phi_2 + \phi_1^* \to \phi_1 + h$	2110
$\phi_1 + \phi_1 \to \phi_2 + h$	1120	$\phi_2 + h \to \phi_1 + \phi_1$	2011

Table 2.1: The $2 \to 2$ processes that are allowed in the $\mathbb{Z}_5$ model and that can modify the relic density of ϕ_1 (left) and ϕ_2 (right). h denotes the SM Higgs boson. Conjugate and inverse processes are not shown.

The table 2.2 (2.3) displays the ϕ_1 annihilation and semi-annihilation (conversion) processes through different channels involving the terms in (2.13). For

Type	Process	Channels
Annihilation	$\phi_1 + \phi_1^* \to h + h$ (1100)	
Semi-annihilation	$\phi_1 + \phi_2 \to \phi_2 + h$ (1220) $\phi_1 + \phi_1 \to \phi_2^* + h$ (1120) $\phi_1 + h \to \phi_2 + \phi_2$ (1022)	

Table 2.2: DM annihilation and semi-annihilation processes via qubic and quartic interactions involving the characteristic parameters of $\mathbb{Z}_5$ symmetry. The notation 0, 1 and 2 corresponds to the fields h, $\phi_1(\phi_1^*)$ and $\phi_2(\phi_2^*)$, respectively

ϕ_2, we can replace $\lambda_{S1} \to \lambda_{S2}$, $\mu_{S1} \to \mu_{S2}$ and $\lambda_{31} \to \lambda_{32}$. The relic abundance of

DM may be computed by using (1.7), and taking into account all the processes

that modify the numeric density of ϕ_i in the early universe (all the processes

Type	Process	Channels

Conversion

$\phi_1 + \phi_1^* \rightarrow \phi_2 + \phi_2^*$

(1122)

$\phi_1 \quad\quad\quad h \quad\quad\quad \phi_2$
$\phi_1^* \quad \sim \lambda_{S1}\lambda_{S2}v_H^2 \quad \phi_2^*$

$\phi_1 \quad\quad\quad\quad\quad \phi_2^*$
$\phi_1 \quad\quad \phi_1 \quad\quad \quad$
$\phi_1^* \quad \sim |\mu_{S1}|^2 \quad \phi_2$

$\phi_1 \quad\quad\quad\quad\quad \phi_2$
$\quad\quad \phi_2 \quad\quad$
$\phi_1^* \quad \sim |\mu_{S2}|^2 \quad \phi_2^*$

$\phi_1 \quad\quad\quad\quad\quad \phi_2$
$\phi_1^* \quad \sim \lambda_{412} \quad \phi_2^*$

$\phi_1 + \phi_2^* \rightarrow \phi_2^* + \phi_2^*$

(1222)

$\phi_1 \quad\quad \phi_1 \quad\quad \phi_2^*$
$\phi_2^* \quad \sim \mu_{S1}\mu_{S2}^* \quad \phi_2^*$

$\phi_1 \quad\quad\quad\quad\quad \phi_2^*$
$\quad\quad \phi_1 \quad\quad$
$\phi_2^* \quad \sim \mu_{S1}\mu_{S2}^* \quad \phi_2^*$

$\phi_1 \quad\quad\quad\quad\quad \phi_2^*$
$\phi_2^* \quad \sim \lambda_{32} \quad \phi_2^*$

$\phi_1 + \phi_1 \rightarrow \phi_1 + \phi_2$

(1112)

$\phi_1 \quad\quad\quad\quad\quad \phi_1$
$\quad\quad \phi_2 \quad\quad$
$\phi_1 \quad \sim \mu_{S1}\mu_{S2} \quad \phi_2$

$\phi_1 \quad\quad\quad\quad\quad \phi_1$
$\quad\quad \phi_2 \quad\quad$
$\phi_1 \quad \sim \mu_{S1}\mu_{S2} \quad \phi_2$

$\phi_1 \quad\quad\quad\quad\quad \phi_1$
$\phi_1 \quad \sim \lambda_{31} \quad \phi_2$

Table 2.3: DM conversion processes via cubic and quartic interactions involving the characteristic parameters of $\mathbb{Z}_5$ symmetry. The notation 0, 1 and 2 corresponds to the fields h, $\phi_1(\phi_1^*)$ and $\phi_2(\phi_2^*)$, respectively.

shown in these tables). Thus, the Boltzmann equation for ϕ_1 reads

$$\frac{dn_1}{dt} = \underbrace{-\sigma_v^{1100}\left(n_1^2 - \bar{n}_1^2\right)}_{\substack{\text{annihilation of } \phi_1 \\ \text{into SM particles}}}$$

$$\underbrace{-\frac{1}{2}\sigma_v^{1220}\left(n_1 n_2 - n_2 \bar{n}_1\right) - \sigma_v^{1120}\left(n_1^2 - n_2 \frac{\bar{n}_1^2}{\bar{n}_2}\right) + \frac{1}{2}\sigma_v^{1022}\left(n_2^2 - n_1 \frac{\bar{n}_2^2}{\bar{n}_1}\right)}_{\text{semi-annihilation of } \phi_1 \text{ into } \phi_2 \text{ or SM particles}}$$

$$\underbrace{-\sigma_v^{1122}\left(n_1^2 - n_2^2 \frac{\bar{n}_1^2}{\bar{n}_2^2}\right) - \frac{1}{2}\sigma_v^{1222}\left(n_1 n_2 - n_2^2 \frac{\bar{n}_1}{\bar{n}_2}\right) - \frac{1}{2}\sigma_v^{1112}\left(n_1^2 - n_1 n_2 \frac{\bar{n}_1}{\bar{n}_2}\right)}_{\text{conversion of } \phi_1 \text{ into } \phi_2}$$

$$- 3H n_1, \tag{2.14}$$

where we adopted the notation followed in [43]: the numbers 0, 1, and 2 correspond to the SM sector, ϕ_1, and ϕ_2 DM particles respectively. $\langle\sigma_{ab\to cd}|v|\rangle \equiv \sigma_v^{abcd}$, and $n_i^{\text{EQ}} \equiv \bar{n}_i$. In addition, we use the fact that

$$\bar{n}_a \bar{n}_b \sigma_v^{abcd} = \bar{n}_c \bar{n}_d \sigma_v^{cdab}. \tag{2.15}$$

Similarly, the Boltzmann equation for ϕ_2 can be constructed only by changing $1 \leftrightarrow 2$ in (2.14). Thus, we have

$$\frac{dn_2}{dt} = \underbrace{-\sigma_v^{2200}\left(n_2^2 - \bar{n}_2^2\right)}_{\substack{\text{annihilation of } \phi_2 \\ \text{into SM particles}}}$$

$$\underbrace{-\frac{1}{2}\sigma_v^{1210}\left(n_1 n_2 - n_1 \bar{n}_2\right) + \frac{1}{2}\sigma_v^{2011}\left(n_1^2 - n_2 \frac{\bar{n}_1^2}{\bar{n}_2}\right) - \sigma_v^{2210}\left(n_2^2 - n_1 \frac{\bar{n}_2^2}{\bar{n}_1}\right)}_{\text{semi-annihilation of } \phi_2 \text{ into } \phi_1 \text{ or SM particles}}$$

$$\underbrace{-\sigma_v^{2211}\left(n_2^2 - n_1^2\frac{\bar{n}_2^2}{\bar{n}_1^2}\right) - \frac{1}{2}\sigma_v^{1211}\left(n_1 n_2 - n_1^2\frac{\bar{n}_2}{\bar{n}_1}\right) - \frac{1}{2}\sigma_v^{2221}\left(n_2^2 - n_1 n_2\frac{\bar{n}_2}{\bar{n}_1}\right)}_{\text{conversion of }\phi_2\text{ into }\phi_1}$$

$$- 3Hn_2. \tag{2.16}$$

According to the characteristic terms displayed in the tables 2.2 and 2.3, we can compute the thermally averaged cross-section at tree level. For ϕ_1 annihilations, taking $M_1 >> M_h$, we neglect the s,t-channels and it only acquires contribution from the quartic interaction,

$$\sigma_v^{1100} \sim \frac{\lambda_{S1}^2}{16\pi M_1^2}. \tag{2.17}$$

Therefore, the annihilation regime increases as λ_{S1}.

As we saw, the semi-annihilation regime is governed by the trilinear couplings μ_{Si}. Assuming $\lambda_{S2} << \lambda_{S1}$, we neglect the channels dependents of $\mu_{Si}\lambda_{S2}v_H$; also setting $M_1 << M_h$, this gives thermally averaged cross sections such as

$$\sigma_v^{1220} \sim \frac{|\mu_{S2}|^2\lambda_{S1}^2 v_H^2}{16\pi M_1^6}, \quad \sigma_v^{1120} \sim \frac{|\mu_{S1}|^2\lambda_{S1}^2 v_H^2}{16\pi M_1^6}, \quad \sigma_v^{1022} \sim \frac{|\mu_{S2}|^2\lambda_{S1}^2 v_H^2}{16\pi M_1^6}, \tag{2.18}$$

being then ξ^{semi} strongly dependent of the M_1 value: lower values of M_1 imply that the semi-annihilations processes dominate.

On the other hand, the conversion processes involve the new trilinear and quartic terms at once. However, if we assume $\lambda_{S2} << \lambda_{S1}$, $M_1 >> M_h$ and

$\lambda_{3i} = 0$, the following dependence is obtained:

$$\sigma_v^{1122} \sim \frac{\lambda_{412}^2}{16\pi M_1^2},$$ (2.19)

so that the DM conversion rate increases according to λ_{412}, and such as the previous processes, it depends on M_1.

In [43], the above discussion is summarized by analyzing the figure 2.1 where ξ_{anni}^i, ξ_{semi}^i, and ξ_{conv}^i are the annihilation, semi-annihilation and conversion rates of ϕ_i respectively; of course, $\xi_{anni}^i + \xi_{semi}^i + \xi_{conv}^i = 1$. These quantities were calculated by solving the equations (2.14) and (2.16) through a scan on the parameter space, running each parameter in a specific interval (see section 4.1 for a detailed description of the scan). Notice that low values of M_1 imply increments in the annihilation fraction, intermediate values increase the semi-annihilation fraction and high values lead to high conversion rates.
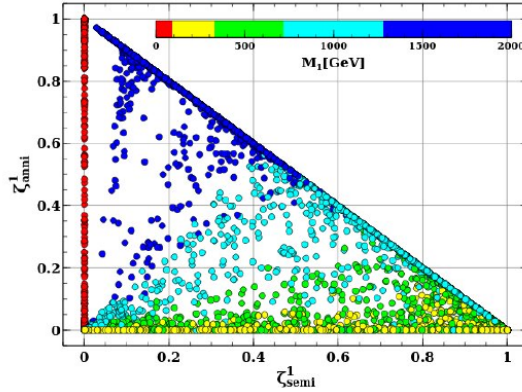
Figure 2.1: Semi-annihilation and annihilation fractions with the M_1 value plotted as the color-code. The figure was taken from [43].

3

Theoretical bounds

The theoretical bounds consist of a set of mathematical constraints that come from the quantum field theory and give theoretic sense to the model. In addition to experimental constraints, we must ensure that the model fulfills the following restrictions:

- Perturbativity

- Unitarity

- Positivity of the scalar potential

- Stability of the scalar potential

We can find in the literature research as [37, 44] which impose these kind of constraints on specific $\mathbb{Z}_N$ models. In the following, we present each restriction mentioned above and its mathematical consistency.

3.1 POSITIVITY

Ensuring the positivity of the scalar potential means maintaining its bound from below for each point in the parameter space. This can be fulfilled if we guarantee the *copositivity* of the coupling matrix. Researches like [45, 46] show the conditions for that purpose. For this model, we have different cases to ensure positivity. In the case $\lambda_{3i} = 0$ expressing $|H| = h$ and $\phi_i = \varphi_i e^{i\theta_i}$, we have that the scalar potential for quartic terms can be expressed as

$$\mathcal{V}_{\mathbb{Z}_5}^{(4)} = \frac{1}{2} \begin{pmatrix} h^2 & \varphi_1^2 & \varphi_2^2 \end{pmatrix} \begin{pmatrix} 2\lambda_H & \lambda_{S1} & \lambda_{S2} \\ \lambda_{S1} & 2\lambda_{41} & \lambda_{412} \\ \lambda_{S2} & \lambda_{412} & 2\lambda_{42} \end{pmatrix} \begin{pmatrix} h^2 \\ \varphi_1^2 \\ \varphi_2^2 \end{pmatrix}, \tag{3.1}$$

where we obtain the following constraints for the copositivity of the above coupling matrix,

$$\lambda_H > 0, \lambda_{4i} > 0,$$

$$\Lambda_i \equiv \lambda_{Si} + 2\sqrt{\lambda_H \lambda_{4i}} \geq 0, \Lambda_3 \equiv \lambda_{412} + 2\sqrt{\lambda_{41}\lambda_{42}} \geq 0, \tag{3.2}$$

$$2\sqrt{\lambda_H \lambda_{41} \lambda_{42}} + \lambda_{S1}\sqrt{\lambda_{42}} + \lambda_{S2}\sqrt{\lambda_{41}} + \lambda_{412}\sqrt{\lambda_H} + \sqrt{\Lambda_1 \Lambda_2 \Lambda_3} \geq 0,$$

Notice that the positivity conditions do not take into account any dimensionful parameter, then this only restricts the dimensionless couplings.

On the other hand, the case $\lambda_{3i} \neq 0$, again with $|H| = h$ and $\phi_i = \varphi_i e^{i\theta_i}$, the

quartic potential reads

$$\mathcal{V}_4 = \lambda_H h^4 + \lambda_{S1} h^2 \varphi_1^2 + \lambda_{41} \varphi_1^4 + \lambda_{42} \varphi_2^4 + \lambda_{S2} h^2 \varphi_2^2 + \lambda_{412} \varphi_1^2 \varphi_2^2$$

$$+ \lambda_{31} \varphi_1^3 \varphi_2 \cos\theta_+ + \lambda_{32} \varphi_1 \varphi_2^3 \cos\theta_-,$$

where $\theta_+ = 3\theta_1 + \theta_2$ and $\theta_- = \theta_1 - 3\theta_2$.

According to [45,46], when the three scalar fields are non-zero, we obtain the following conditions:

$$\lambda_{4i} > 0, D > 0 \wedge (Q > 0 \vee R > 0), \tag{3.3}$$

where

$$D = -27\lambda_{42}^2 |\lambda_{31}|^4 - 4|\lambda_{32}|^3 |\lambda_{31}|^3 + 18|\lambda_{32}|\lambda_{42}\lambda_{412}|\lambda_{31}|^3$$

$$- 4\lambda_{42}\lambda_{412}^3 |\lambda_{31}|^2 + |\lambda_{32}|^2 \lambda_{412}^2 |\lambda_{31}|^2 - 6|\lambda_{32}|^2 \lambda_{41}\lambda_{42}|\lambda_{31}|^2$$

$$+ 144\lambda_{41}\lambda_{42}^2 \lambda_{412}|\lambda_{31}|^2 - 192|\lambda_{32}|\lambda_{41}^2 \lambda_{42}^2 |\lambda_{31}| - 80|\lambda_{32}|\lambda_{41}\lambda_{42}\lambda_{412}^2 |\lambda_{31}|$$

$$+ 18|\lambda_{32}|^3 \lambda_{41}\lambda_{412}|\lambda_{31}| + 16\lambda_{41}\lambda_{42}\lambda_{412}^4 + 256\lambda_{41}^3 \lambda_{42}^3 - 4|\lambda_{32}|^2 \lambda_{41}\lambda_{412}^3$$

$$- 27|\lambda_{32}|^4 \lambda_{41}^2 - 128\lambda_{41}^2 \lambda_{42}^2 \lambda_{412}^2 + 144|\lambda_{32}|^2 \lambda_{41}^2 \lambda_{42}\lambda_{412}, \tag{3.4}$$

$$Q = 8\lambda_{41}\lambda_{412} - 3|\lambda_{31}|^2, \tag{3.5}$$

$$R = -3|\lambda_{31}|^4 + 16\lambda_{41}\lambda_{412}|\lambda_{31}|^2 + 64\lambda_{41}^3 \lambda_{42} - 16\lambda_{41}^2 \left(\lambda_{412}^2 + |\lambda_{31}||\lambda_{32}|\right). \tag{3.6}$$

If λ_{Si} are allowed to take negative values, new conditions are added. The

case $\lambda_{Si} < 0$ leads to

$$4\lambda_H\lambda_{4i} - \lambda_{Si}^2 > 0 \wedge \left[\tilde{D} > 0 \wedge \left(\tilde{Q} > 0 \vee \tilde{R} > 0\right)\right], \tag{3.7}$$

where $\tilde{D}$, $\tilde{Q}$ and $\tilde{R}$ being D, Q and R with $\lambda_{4i} \to \lambda_{4i} - \lambda_{Si}^2/(4\lambda_H)$ and $\lambda_{412} \to \lambda_{412} - \lambda_{S1}\lambda_{S2}/(2\lambda_H)$.

Finally, for the case $\lambda_{S1}\lambda_{S2} < 0$, arise the following conditions:

$$\lambda'_{4i} > 0 \wedge \left\{\left[\tilde{D} \leq 0 \vee \left(\lambda'_{31}\,(\lambda'_{42})^{1/2} + \lambda'_{32}(\lambda'_{41})^{1/2}\right) > 0\right]\right.$$
$$\vee \left[-2\,(\lambda'_{41}\lambda'_{42})^{1/2} < \lambda'_{412} < 6\,(\lambda'_{41}\lambda'_{42})^{1/2} \wedge \tilde{D} \geq 0 \wedge \Lambda'_1 \leq 0\right]$$
$$\left.\vee \left[6\,(\lambda'_{41}\lambda'_{42})^{1/2} < \lambda'_{412} \wedge \left((\lambda'_{31} > 0 \wedge \lambda'_{32} > 0) \vee \left(\tilde{D} \geq 0 \wedge \Lambda'_2 \leq 0\right)\right)\right]\right\}, \tag{3.8}$$

where

$$\lambda'_{41} = \lambda_H \left(\lambda_{42}\lambda_{S1}^2 - \lambda_{412}\lambda_{S1}\lambda_{S2} + \lambda_{41}\lambda_{S2}^2\right.$$
$$\left.-\sqrt{|\lambda_{S1}\lambda_{S2}|}\,(|\lambda_{32}|\,|\lambda_{S1}| + |\lambda_{31}|\,|\lambda_{S2}|)\right), \tag{3.9}$$

$$\lambda'_{31} = 2\lambda_H\mathrm{sgn}(\lambda_{S2} - \lambda_{S1})\left(2\lambda_{42}\lambda_{S1}^2 - 2\lambda_{41}\lambda_{S2}^2\right.$$
$$\left.-\sqrt{|\lambda_{S1}\lambda_{S2}|}\,(|\lambda_{32}|\,|\lambda_{S1}| - |\lambda_{31}|\,|\lambda_{S2}|)\right), \tag{3.10}$$

$$\lambda'_{412} = 2\lambda_H\left(3\lambda_{42}\lambda_{S1}^2 + \lambda_{412}\lambda_{S1}\lambda_{S2} + 3\lambda_{41}\lambda_{S2}^2\right) - 4\lambda_{S1}^2\lambda_{S2}^2, \tag{3.11}$$

$$\lambda'_{32} = 2\lambda_H\mathrm{sgn}(\lambda_{S2} - \lambda_{S1})\left(2\lambda_{42}\lambda_{S1}^2 - 2\lambda_{41}\lambda_{S2}^2\right.$$
$$\left.+\sqrt{|\lambda_{S1}\lambda_{S2}|}\,(|\lambda_{32}|\,|\lambda_{S1}| - |\lambda_{31}|\,|\lambda_{S2}|)\right), \tag{3.12}$$

$$\lambda'_{42} = \lambda_H\left(\lambda_{42}\lambda_{S1}^2 - \lambda_{412}\lambda_{S1}\lambda_{S2} + \lambda_{41}\lambda_{S2}^2\right.$$

$$+\sqrt{|\lambda_{S1}\lambda_{S2}|}\left(|\lambda_{32}|\,|\lambda_{S1}| + |\lambda_{31}|\,|\lambda_{S2}|\right), \tag{3.13}$$

and

$$\Lambda'_1 = \left[(\lambda'_{42})^{1/2}\lambda'_{31} - \lambda'_{32}(\lambda'_{41})^{1/2}\right]^2 - 32\left(\lambda'_{42}\lambda'_{41}\right)^{3/2}$$

$$- 16\left[\lambda'_{41}\lambda'_{412}\lambda'_{42} + (\lambda'_{41})^{3/4}\lambda'_{31}(\lambda'_{42})^{5/4} + (\lambda'_{42})^{3/4}\lambda'_{32}(\lambda'_{41})^{5/4}\right], \tag{3.14}$$

$$\Lambda'_2 = \left((\lambda'_{42})^{1/2}\lambda'_{31} - \lambda'_{32}(\lambda'_{41})^{1/2}\right)^2 - 4\left(\lambda'_{42}\lambda'_{41}\right)^{1/2}\left(\lambda'_{412} + 2\left(\lambda'_{41}\lambda'_{42}\right)^{1/2}\right)$$

$$\times \left[(\lambda'_{42})^{1/2}\lambda'_{31} + (\lambda'_{41})^{1/2}\lambda'_{32} + 4\left(\lambda'_{41}\lambda'_{42}\right)^{1/2}\left(\lambda'_{412} - 2\left(\lambda'_{41}\lambda'_{42}\right)^{1/2}\right)^{1/2}\right]$$

$$\times \left(\lambda'_{412} - 2\left(\lambda'_{41}\lambda'_{42}\right)^{1/2}\right)^{-1/2}. \tag{3.15}$$

3.2 PERTURBATIVE UNITARITY

As is known, in a classic paper Lee, Quigg, and Tracker (see e.g., [47]) showed that in order to maintain perturbative unitarity, the Higgs mass has to be below 1 TeV. This means that the bounds which impose the perturbative unitarity allow restricting the free parameters of the theory. The S-Matrix of the model has to maintain unitary for all the viable points in the parameter space. In that sense,

$$SS^\dagger = 1. \tag{3.16}$$

Neglecting the non interacting processes, as is usual, we define $S = 1 + iT$. This leads to

$$-i(T - T^\dagger) = TT^\dagger, \tag{3.17}$$

which expresses the probability conservation. Thus, ensuring the unitarity of S-Matrix leads to probability conservation. Research like [47,48] shows that this can be easily ensured if we impose over the eigenvalues a_i of the S-Matrix, the condition

$$|\text{Re}\,(a_i)| \leq \frac{1}{2}. \tag{3.18}$$

For a pair a of scalars which scatters to another pair b, it can be computed as [44]

$$a^{ba} = \frac{1}{32\pi} \sqrt{\frac{2|\boldsymbol{p}^b||\boldsymbol{p}^a|}{2^{\delta_{12}} 2^{\delta_{34}} s}} \int_{-1}^{1} d(\cos\theta)\, \mathcal{M}_{ba}(\cos\theta) P_0(\cos\theta). \tag{3.19}$$

Of course, these eigenvalues depend on the center-of-mass energy, as we can see. Rarely in the literature we may find this kind of analysis with s finite, usually we found that for $s \to \infty$. In this research, we impose perturbative unitarity for s finite, setting $\sqrt{s} \geq 2M_2$ to avoid spurious poles. For more details, see section 4.3 where is explained the conditions that must fulfill s to keep the physical sense of the model.

We implemented the model in `SARAH 4.14.4` to obtain the S-Matrix entries. This matrix contains all the information about the scattering amplitudes, which in this case has 36 entries. We found that the condition (3.18) leads, in the limit

of large-s at tree-level and setting $\lambda_{3i} = \mu_{Si} = 0$, to the following constraints:

$$\lambda_{Si} < 8\pi,$$

$$\left| 2\lambda_{4i} + \lambda_{412} \pm \sqrt{18\lambda_{3i}^2 + (2\lambda_{4i} - \lambda_{412})^2} \right| < 16\pi, \qquad (3.20)$$

$$|\alpha_{1,2,3}| \leq 1/2,$$

where α_i are the roots of the polynomial $c_3 x^3 + c_2 x^2 + c_1 x + c_0$ with

$$c_0 = 2v_H^2 \left(-3\lambda_{412}^2 \lambda_H + \lambda_{41} \left(48\lambda_{42}\lambda_H - 4\lambda_{S2}^2 \right) - 4\lambda_{42}\lambda_{S1}^2 + 2\lambda_{412}\lambda_{S1}\lambda_{S2} \right),$$

$$c_1 = 6\pi v_H^2 \left(24 \left(\lambda_{41} + \lambda_{42} \right) \lambda_H - \lambda_{412}^2 + 16\lambda_{41}\lambda_{42} - 2 \left(\lambda_{S1}^2 + \lambda_{S2}^2 \right) \right),$$

$$c_2 = 512\pi^2 v_H^2 \left(3\lambda_H + 2 \left(\lambda_{41} + \lambda_{42} \right) \right),$$

$$c_3 = 4096\pi^3 v_H^2. \qquad (3.21)$$

In the scan development, the general conditions will be considered for a better review of the constraints on the model.

3.3 STABILITY

Among the minima of the scalar potential, we have several cases that must be analyzed. The main condition that we must guarantee about those minima is that the SM minimum be the global minimum of the theory. The different minima are showed in the following for the cases in that EW symmetry is broken or the $\mathbb{Z}_5$ is broken, i.e., $\langle \phi_1 \rangle = v_1 \neq 0$ or $\langle \phi_2 \rangle = v_2 \neq 0$:

- $\mathcal{M}_A:$ $v_H^2 = 0,$ $v_i^2 = 0.$

- $\mathcal{M}_B:$ $v_H^2 = 0,$ $v_i^2 \neq 0,$ $v_j^2 = 0,$ for $i \neq j.$

- $\mathcal{M}_C:$ $v_H^2 = 0,$ $v_i^2 \neq 0.$

- $\mathcal{M}_D:$ $v_H^2 \neq 0,$ $v_i^2 \neq 0,$ $v_j^2 = 0,$ for $i \neq j.$

- $\mathcal{M}_E:$ $v_H^2 \neq 0,$ $v_i^2 = 0.$

- $\mathcal{M}_F:$ $v_H^2 \neq 0,$ $v_i^2 \neq 0.$

We have then eight different minima. The first four minima are ruled out since they do not lead to SM-like minima, while those with $v_i^2 \neq 0$ do not allow multi-component DM, thus we are left with the minimum $\mathcal{M}_E$ where EW symmetry is broken and $\mathbb{Z}_5$ symmetry is conserved. The minimum of the potential turns to be then

$$\left. \mathcal{V}_{\mathbb{Z}_5} \right|_{\mathcal{M}_E} = -\frac{\mu_H^4}{4\lambda_H}, \tag{3.22}$$

and must fulfill

$$\left. \mathcal{V}_{\mathbb{Z}_5} \right|_{\mathcal{M}_E} < \left. \mathcal{V}_{\mathbb{Z}_5} \right|_{\mathcal{M}_{A,B,C,D,F}} \tag{3.23}$$

to be the global extremum.

The most important minimum is $\mathcal{M}_F$ since it contains all the conditions for the other minima. Of course, the solution for this is not analytical, but we can develop a numerical solution, solving the following two coupled equations for

v_i^2 and v_j^2 (with $i \neq j$),

$$\frac{\partial \mathcal{V}}{\partial \phi_i} = 0 = 4\lambda_{4i}v_i^3 + 3\lambda_{3i}v_iv_j^2 + v_i \left(v_H^2\lambda_{Si} + 2\mu_i^2 + 2v_j\mu_{Si} + 2\lambda_{412}v_j^2 \right)$$

$$+ v_2^2 \left(\mu_{Sj} + \lambda_{3j}v_j \right), \tag{3.24}$$

and after of that, (3.23) must be fulfilled taking into account the fixed value for the SM-minimum given in (3.22).

3.4 RGEs running

The Renormalization Group Equation (RGEs) are a set of coupled differential equations that describe the behavior at different energy scales for each parameter of the model. We calculated the RGEs at 2-loop level by implementing the model in `SARAH 14.4.4`. The expressions are:

$$\beta_{\lambda_{4i}}^{(2)} = 3\lambda_{3j}^2 \left(\lambda_{4i} - 3\lambda_{412} \right) - 9\lambda_{3i}^2 \left(11\lambda_{4i} + 3\lambda_{412} \right) - \frac{2}{5} \left(-6g_1^2\lambda_{Si}^2 - 30g_2^2\lambda_{Si}^2 \right.$$

$$\left. + 600\lambda_{4i}^3 + 25\lambda_{412}^2\lambda_{4i} + 10\lambda_{412}^3 + 50\lambda_{4i}\lambda_{Si}^2 + 20\lambda_{Si}^3 \right), \tag{3.25}$$

$$\beta_{\lambda_{Si}}^{(2)} = \frac{72}{5}g_1^2\lambda_H\lambda_{Si} + 72g_2^2\lambda_H\lambda_{Si} + \frac{1671}{400}g_1^4\lambda_{Si} + \frac{3}{5}g_1^2\lambda_{Si}^2 + \frac{9}{8}g_2^2g_1^2\lambda_{Si}$$

$$+ 3g_2^2\lambda_{Si}^2 - \frac{145}{16}g_2^4\lambda_{Si} - 72\lambda_H\lambda_{Si}^2 - 60\lambda_H^2\lambda_{Si} - 11\lambda_{Si}^3$$

$$- 48\lambda_{4i}\lambda_{Si}^2 - 40\lambda_{4i}^2\lambda_{Si} - \lambda_{412}^2\lambda_{Si} - \lambda_{Si}\lambda_{Sj}^2 - 8\lambda_{412}\lambda_{Si}\lambda_{Sj}$$

$$- \frac{9}{2}\lambda_{3i}^2 \left(3\lambda_{Si} + 2\lambda_{Sj} \right) + \frac{3}{2}\lambda_{3j}^2 \left(\lambda_{Si} - 6\lambda_{Sj} \right) - 4\lambda_{412}\lambda_{Sj}^2 - 4\lambda_{412}^2\lambda_{Sj}, \tag{3.26}$$

$$\beta_{\lambda_{412}}^{(2)} = \frac{72}{5}g_1^2\lambda_H\lambda_{S2} + 72g_2^2\lambda_H\lambda_{S2} + \frac{1671}{400}g_1^4\lambda_{S2} + \frac{3}{5}g_1^2\lambda_{S2}^2 + \frac{9}{8}g_2^2g_1^2\lambda_{S2}$$

$$+ 3g_2^2\lambda_{S2}^2 - \frac{145}{16}g_2^4\lambda_{S2} - 72\lambda_H\lambda_{S2}^2 - 60\lambda_H^2\lambda_{S2} - 4\lambda_{412}^2\lambda_{S1}^2$$

$$- 4\lambda_{412}^2\lambda_{S1} - \lambda_{S1}^2\lambda_{S2} - 8\lambda_{412}\lambda_{S1}\lambda_{S2} + \frac{3}{2}\lambda_{31}^2\left(\lambda_{S2} - 6\lambda_{S1}\right)$$

$$- \frac{9}{2}\lambda_{32}^2\left(2\lambda_{S1} + 3\lambda_{S2}\right) - 11\lambda_{S2}^3 - 48\lambda_{42}\lambda_{S2}^2 - 40\lambda_{42}^2\lambda_{S2} - \lambda_{412}^2\lambda_{S2}, \quad (3.27)$$

$$\beta_{\lambda_H}^{(2)} = -\frac{9}{5}g_1^2\lambda_H - 9g_2^2\lambda_H + \frac{1}{16\pi^2}\left(\frac{1887}{200}g_1^4\lambda_H + \frac{108}{5}g_1^2\lambda_H^2 + \frac{117}{20}g_2^2g_1^2\lambda_H\right.$$

$$+ 108g_2^2\lambda_H^2 - \frac{73}{8}g_2^4\lambda_H + \frac{17}{2}g_1^2\lambda_H y_t^2 + \frac{45}{2}g_2^2\lambda_H y_t^2 + 80g_3^2\lambda_H y_t^2 - \frac{171}{100}g_1^4 y_t^2$$

$$- \frac{8}{5}g_1^2 y_t^4 + \frac{63}{10}g_2^2g_1^2 y_t^2 - 32g_3^2 y_t^4 - \frac{9}{4}g_2^4 y_t^2 - \frac{3411g_1^6}{2000} - \frac{1677}{400}g_2^2g_1^4 - \frac{289}{80}g_2^4g_1^2$$

$$+ \frac{305g_2^6}{16} - 312\lambda_H^3 - 10\lambda_H\lambda_{S1}^2 - 10\lambda_H\lambda_{S2}^2 - 144\lambda_H^2 y_t^2 - 3\lambda_H y_t^4 - 4\lambda_{S1}^3$$

$$\left. -4\lambda_{S2}^3 + 30y_t^6\right) + \frac{27g_1^4}{200} + \frac{9}{20}g_2^2g_1^2 + \frac{9g_2^4}{8} + 24\lambda_H^2 + 12\lambda_H y_t^2 + \lambda_{S1}^2$$

$$+ \lambda_{S2}^2 - 6y_t^4 \quad (3.28)$$

The purpose of this work is to study the mentioned bounds at energy scales from top quark scale ~ 173 GeV to Planck energy scale $\sim 10^{19}$ GeV. With this, we explore the viability of the model, and ensure its consistence at all the energy scales below of Planck energy scale.

4

Results and analysis

In this section, we expose and discuss the results obtained after the implementation of the constraints established in the past section.

4.1 SCAN

Since the majority of the restrictions are not analytic including the RGEs solutions, we are going to do a scan over all the parameter space, running on the intervals suggested in [43].

$$40 \, \text{GeV} \leq M_1 \leq 2 \, \text{TeV},$$

$$M_1 < M_2 < 2M_1,$$

$$10^{-4} \leq \lambda_{4i}, |\lambda_{412,Si,3i}| \leq \sqrt{4\pi}, \quad (4.1)$$

$$100 \, \text{GeV} \leq |\mu_{Si}| \leq 10 \, \text{TeV}.$$

The above intervals are viable to describe a two-component DM scenario.

The scan will be performed initially taking $\lambda_{412} = \lambda_{3i} = \mu_{S2} = 0$. Later, in section 4.7 some results of the scan with these non-zero values are detailed.

Before the implementation of constraints, we must ensure that $\Omega_{DM}h^2$ is within the range mentioned in chapter 1. The calculation of the relic density is found with `micromegas_5.3.35`.

On the other hand, for direct detection experiments, we take into account the bound presented by the PANDAX experiment [30]. In [43], we may find the results of implementing these experimental constraints in order to examine the viable parameter space through a scan in the intervals mentioned above; the figure 4.1 displays these results.
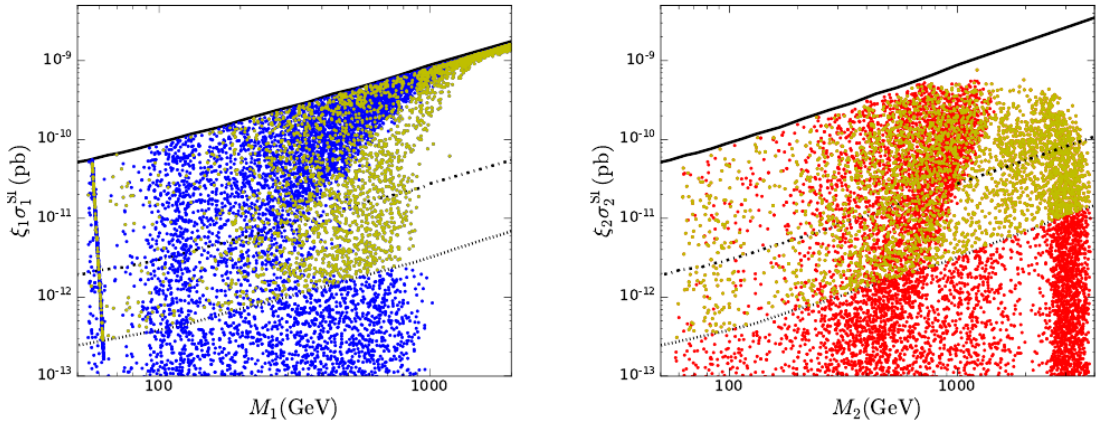
Figure 4.1: Scan results taken from [43] for spin-independent cross-sections for elastic scattering of ϕ_i with nuclei. The factor $\xi_i = \Omega_i/\Omega_{\text{DM}}$ scales the cross-section per particle. The upper limit (solid line) is established by XENON1T collaboration [31], and the projected sensitivity of LZ [29] and DARWIN [49] experiments correspond to the dot-dashed, and dotted lines respectively. Yellow points indicate that both DM particles lay within the sensitivity region of DARWIN.

4.2 PARAMETER SPACE BEHAVIOR THROUGH ENERGY

SCALES

One additional constraint that will be taken into account in the scan, is to guarantee that the parameters remain real to all the energy scales. For this, we neglect the points where a parameter takes complex values, and we store the value of energy scale Λ where this happened as the maximum energy scale Λ_{max} where the model has real parameters. Figure 4.2 shows the results of implementing this constraint. These results (as the next sections) will be compared with the ones obtained in [43], where the constraints considered in this analysis were not taken into account.

The results show that the initially considered parameter space mostly satisfies the condition, however, regions in the plane (λ_{S2}, M_1) show a set of points for λ_{S2} of the order of the unit, which take complex values at $\Lambda \sim 10^8$ GeV, which is a fairly high energy value and therefore not of concern in this study. The aforementioned case can be seen in figure 4.3, where λ_{S2} is restricted according to the energy scale. Additionally, we have considered a set of benchmark points shown in the figures mentioned and listed in the table 4.1. The selected points are such that they are found in extreme places of some of the planes considered, for example, point 2 corresponds to the largest value of the examined mass and shows that the condition considered here is maintained at a large energy scale ($\sim 10^7$ GeV), having a mass of ϕ_1 greater than 1 TeV. On the other hand, the

41

Figure 4.2: Viable parameter space with the real-parameters filter at energy scales up to GUT. The figure shows the free parameters μ_{S1}, $|\lambda_{S1}|$, $|\lambda_{S2}|$ and M_2/M_1 as a function of the mass of ϕ_1. The color code represents the maximum energy scale where the point remains real values for all the parameter space. The benchmark points in the plot are listed in the table 4.1.

region that includes mass values lower than 0.1 TeV shows that there are points

that verify the condition for a wide interval of values of the parameters in figure

4.2.

In summary, the parameter space is not modified by imposing the condition

of maintaining the real values of the parameters, it would only be restricted

considering very large energy scales greater than the order of 10^7 GeV, which is

not of interest for this study.

We can state that most of the space is viable at high energy scales with

Param.	Point 1	Point 2	Point 3	Point 4	Point 5
λ_{41}	0.3475	2.2745	0.0018	0.0321	3.4144
λ_{42}	0.4641	0.0125	3.2527	0.0025	0.3661
λ_{S1}	0.0004	-0.3525	0.0002	0.0014	-0.1967
λ_{S2}	-2.3683	2.1376	3.1533	-0.0002	0.0001
M_1 (GeV)	116.06	1442.11	48.94	59.09	917.92
M_2 (GeV)	123.85	1978.09	52.31	91.87	1069.96
μ_{S1} (GeV)	101.98	9620.26	696.18	4681.35	9986.56
$\Omega_1 h^2$	0.118	0.111	0.113	0.129	0.125
$\Omega_2 h^2$	2.48×10^{-11}	0.0106	1.14×10^{-7}	1.75×10^{-10}	0.0014
$\Omega_{\mathrm{DM}} h^2$	0.118	0.1216	0.113	0.129	0.1264
Ω_1/Ω_2	4.76×10^9	10.4717	9.91×10^5	7.37×10^8	91.24
σ_1^{SI} (pb)	1.12×10^{-13}	5.26×10^{-10}	1.53×10^{-13}	4.50×10^{-12}	4.04×10^{-10}
σ_2^{SI} (pb)	3.18×10^{-6}	1.03×10^{-8}	3.09×10^{-5}	3.28×10^{-14}	1.70×10^{-16}
$\log(\Lambda_{\mathrm{max}}/\mathrm{GeV})$	8.9	6.9	4.9	17.0	8.2

Table 4.1: Benchmark points that fulfill the real-parameters filter up to some energy scale Λ_{max}. The table displays all the free parameters of the model at the top quark mass energy scale, and point 4 is viable at energies beyond of GUT.
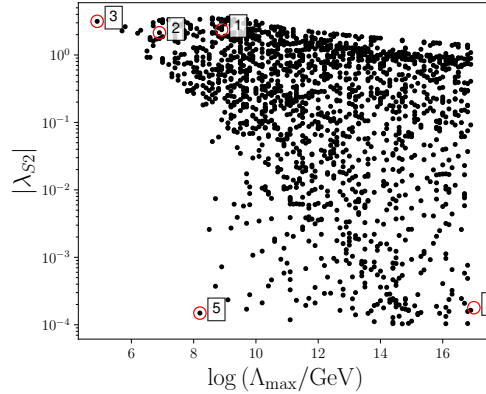
Figure 4.3: Evolution of the viable $|\lambda_{S2}|$ as a function of $\log(\Lambda_{\mathrm{max}}/\mathrm{GeV})$. The figure displays the maximum value of the energy scale for a given point with a specific $|\lambda_{S2}|$ value where all the parameter space remains real.

respect to the constraint of keeping the parameter space real, even though the condition is unsatisfied at certain energy scales, these turn out to be too high to bring phenomenological implications. In addition, the benchmark points do not present recurring characteristics in their values and therefore no specific conditions are established to guarantee the viability of the model space under
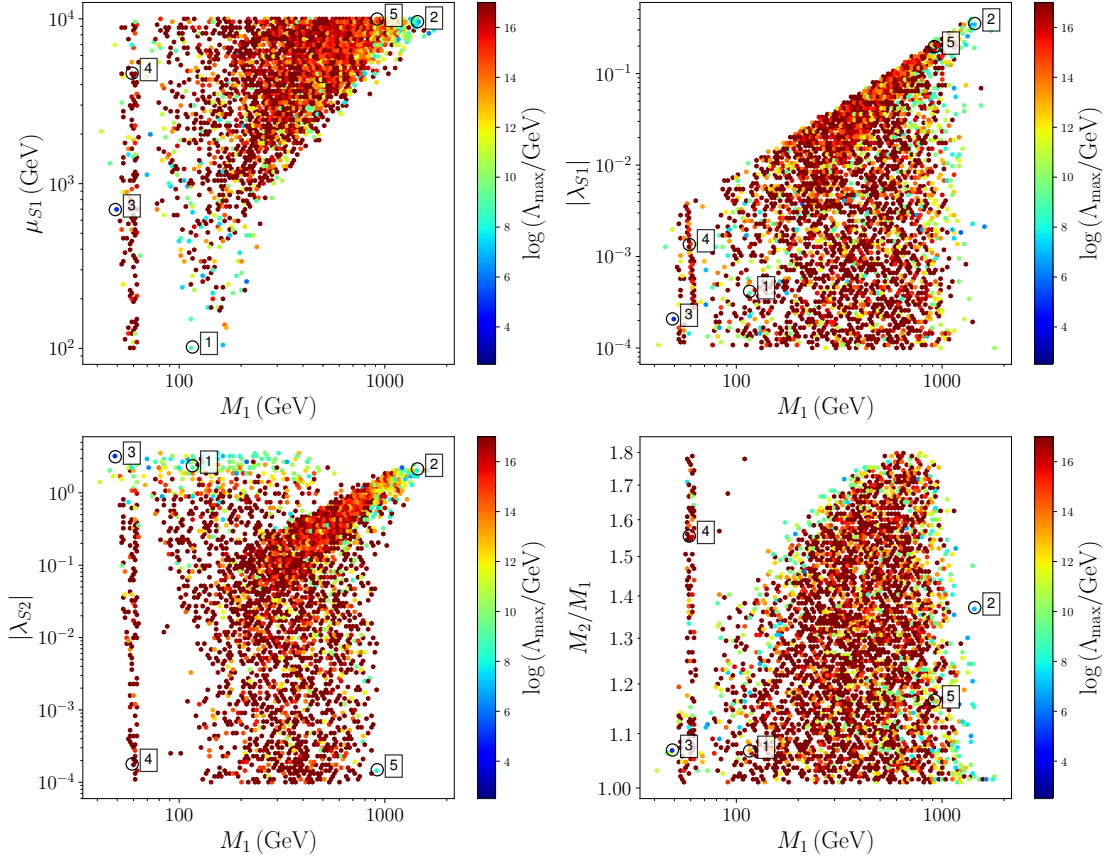
this condition.
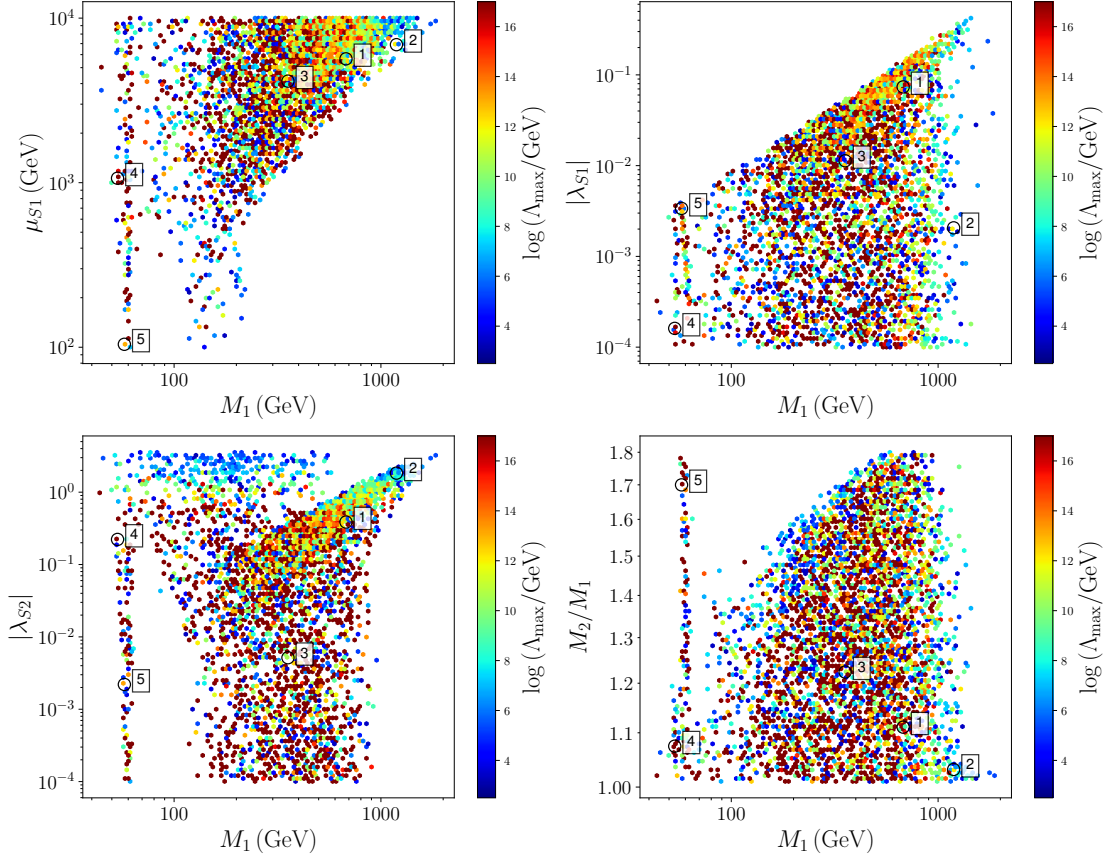
Figure 4.4: Viable parameter space with perturbative unitarity at energy scales up to GUT. The figure shows the free parameters μ_{S1}, $|\lambda_{S1}|$, $|\lambda_{S2}|$ and M_2/M_1 as a function of the mass of ϕ_1. The color code represents the maximum energy scale where the point remains perturbative unitarity unbroken. The benchmark points in the plot are listed in the table 4.2.

4.3 PERTURBATIVE UNITARITY

As mentioned in the previous chapter, perturbative unitarity is a condition that forces the parameter space to keep the scattering matrix unitary in order to guarantee probability conservation. The perturbative unitarity constraints have been calculated via `SARAH_4.14.4`. To avoid spurious poles, the center-of-mass

energy is fixed to $\sqrt{s} = 8\,\mathrm{TeV} > 2M_2$. Most of the works in unitarity set the s-channel at infinity, but it is interesting to check what happens when s decreases to a finite value as is the case. Besides, we implement the perturbative unitarity also at $s \to \infty$ for comparison purposes. Since the perturbative unitarity at finite-s leads to non-analytic expressions, the restrictions presented in (3.20) can not be considered, then we use `Wolfram_Mathematica_13` to compute numerically it.

When implementing the condition (3.18) on the S-matrix, we obtained the results shown in figure 4.4, where as well as the section above, points in the four planes previously considered verify the condition in all regions for several energy scales. Although regions are shown that favor the breaking of the condition at specific energy scales, for instance, $\lambda_{S2} \sim 1$ in the plane $(|\lambda_{S2}|, M_1)$, these scales are considered high since they exceed the order of 10^4 GeV. The benchmark points shown in the mentioned figure are arranged in the table 4.2 and have been chosen in such a way that they are in particular regions of the planes, for instance, point 2 verifies the perturbative unitarity for $M_1 \sim 1$ TeV and breaks said condition at $\Lambda \sim 10^{12}$ GeV. Therefore, it shows the existence of points that fulfill the condition up to high energy scales.

The perturbative unitarity exposes an interesting behavior for the DM self-couplings λ_{4i}, and the Higgs-DM coupling, this is shown in the figure 4.5 where these couplings must take values below the unit to guarantee $\Lambda_{\mathrm{max}} \geq 10^{17}$ GeV. Then this condition forces the values of these couplings to decrease with the en-

Parameter	Point 1	Point 2	Point 3	Point 4	Point 5
λ_{41}	0.0038	0.0002	2.2119	0.2496	0.0284
λ_{42}	0.001	0.0003	1.4049	0.015	0.0002
λ_{S1}	-0.0737	0.0021	-0.0113	0.0002	-0.0034
λ_{S2}	0.3868	-1.8328	0.0052	-0.2223	0.0022
M_1 (GeV)	677.81	1188.96	355.25	53.27	57.48
M_2 (GeV)	753.0	1226.25	434.76	57.24	97.7
μ_{S1} (GeV)	5656.33	6897.21	4140.98	1064.44	104.22
$\Omega_1 h^2$	0.114	0.116	0.123	0.129	0.118
$\Omega_2 h^2$	0.0016	0.0032	0.0002	3.48×10^{-8}	0.0005
$\Omega_{\rm DM} h^2$	0.1156	0.1192	0.1232	0.129	0.1185
Ω_1/Ω_2	69.51	35.69	514.64	3.71×10^{6}	226.92
$\sigma_1^{\rm SI}$ (pb)	1.04×10^{-10}	2.65×10^{-14}	8.91×10^{-12}	7.80×10^{-14}	2.94×10^{-11}
$\sigma_2^{\rm SI}$ (pb)	2.32×10^{-9}	1.97×10^{-8}	1.23×10^{-12}	1.29×10^{-7}	4.38×10^{-12}
$\log(\Lambda_{\rm max}/{\rm GeV})$	17.0	12.0	4.0	17.0	17.0

Table 4.2: Benchmark points that verify the perturbative unitarity condition up to some energy scale $\Lambda_{\rm max}$. The table displays all the free parameters of the model at the top quark mass energy scale, and point 4 is viable at energies beyond of GUT.

ergy scale in order to admit larger scales of viability. The new quartic couplings λ_{3i} also present the same behavior under this constraint.

The results show that the parameter space is not restricted after the implementation of this condition. Most of the regions in the studied planes present several rupture energy scales for the condition. The benchmark points do not make any correlation explicit, we could only mention the fact that $\lambda_{S1}\lambda_{S2} < 0$ at all the benchmark points except point 3, however, this will be studied in detail in the next section.
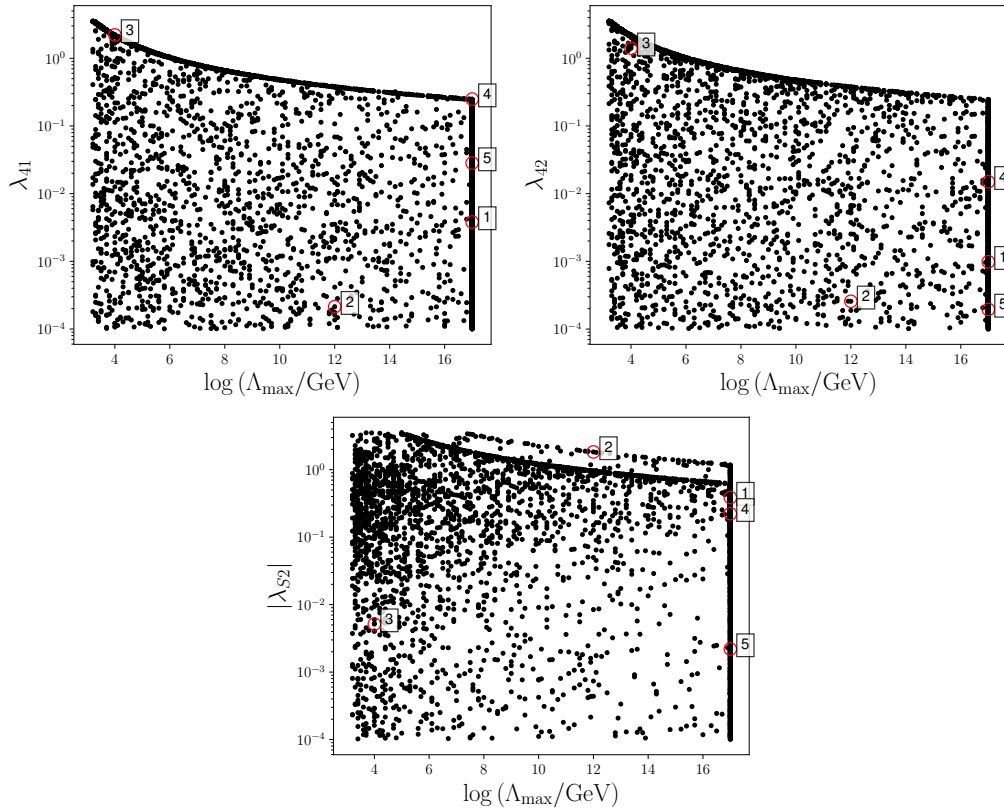
Figure 4.5: Evolution of the viable λ_{41} (top-left), λ_{42} (top-right) and $|\lambda_{S2}|$ (bottom) as a function of $\log(\Lambda_{\mathrm{max}}/\mathrm{GeV})$. The figure displays the maximum value of the energy scale for a given point with specific values of these parameters where the model fulfills the perturbative unitarity bound.

4.4 SCALAR POTENTIAL POSITIVITY

As was exposed in section 3.1, the positivity conditions only restrict the dimensionless (quartic) couplings of the model, so that fixing $\lambda_{3i} = \lambda_{412} = 0$ we obtain conditions with minor complexity than those shown in the previous

chapter. Specifically, taking $\lambda_{412} = 0$ in equation (3.2), we have

$$2\sqrt{\lambda_H \lambda_{41} \lambda_{42}} + \lambda_{S1}\sqrt{\lambda_{42}} + \lambda_{S2}\sqrt{\lambda_{41}}$$
$$+ \sqrt{\left(\lambda_{S1} + 2\sqrt{\lambda_H \lambda_{41}}\right)\left(\lambda_{S2} + 2\sqrt{\lambda_H \lambda_{42}}\right)\left(2\sqrt{\lambda_{41}\lambda_{42}}\right)} \geq 0, \tag{4.2}$$

as well as the vacuum stability conditions $\lambda_H > 0$ and $\lambda_{4i} > 0$. The results of the scan for these conditions are shown in figure 4.6. In this case, the benchmark points chosen are viable points beyond of GUT energy scale except for point 5 which breaks positivity at $\sim 10^{13}$ GeV. The figure shows that the parameter space fulfills positivity in several regions. The color code in the top-left plot suggests that the positivity is mainly guaranteed at $0.1 \lesssim |\lambda_{S2}| \lesssim 1$, for values of M_1 less than ~ 300 GeV. Point 3 was chosen as the point with a greater value of mass, with positivity fulfilled at the GUT energy scale. In summary, the parameter space presents viability under this condition in all the regions and mass ranges initially considered. Some regions privilege certain energy scales like the ones mentioned above, but these scales are too large to imply a significant restriction to the parameter space. Future works that are concerned with analyzing the restrictions of the model to $\Lambda \sim 10^{17}$ GeV, can consider these regions as the admitted ones.

We have some points where $\lambda_H(\Lambda_{\max}) < 0$ which can be interpreted as the green dots of the color code in the figure 4.6. We selected some of these points in order to study the evolution of λ_H with the solution of RGEs, and store each value that takes this coupling at the different Λ-energy scales. The figure 4.7
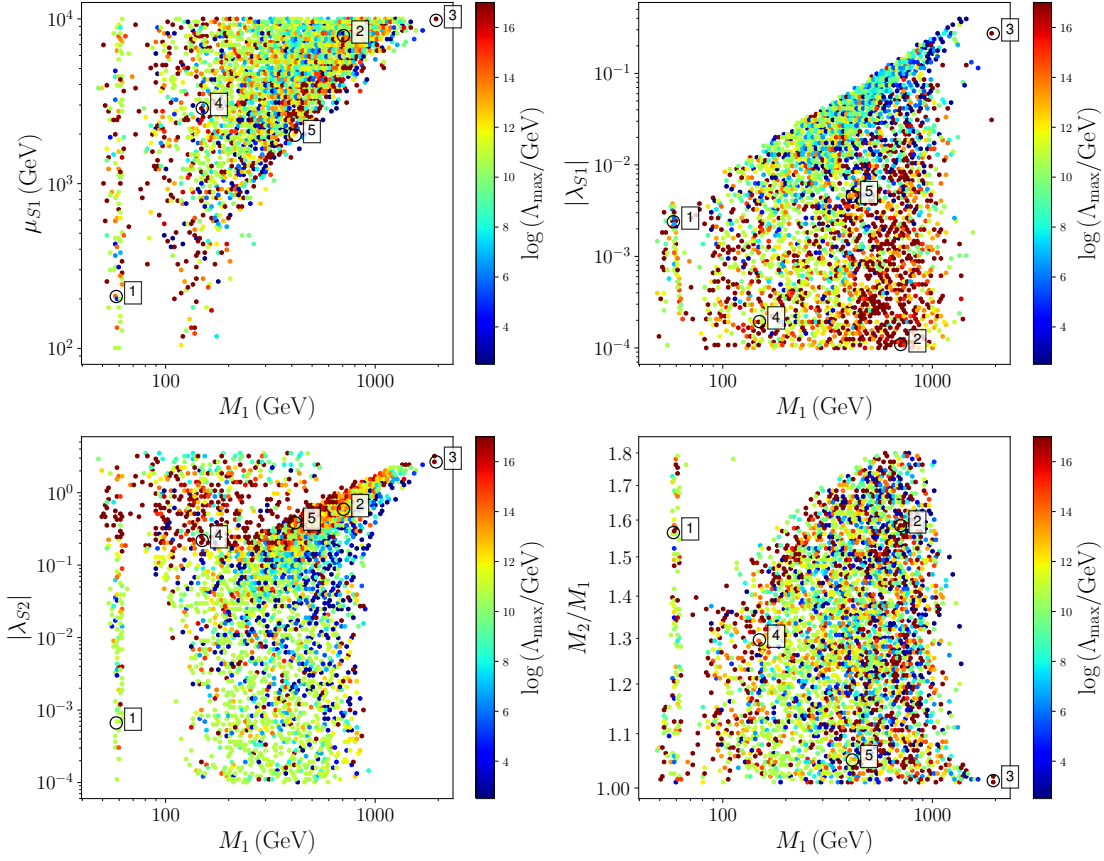
Figure 4.6: Viable parameter space with scalar potential positivity at energy up to GUT scale. The figure shows the free parameters μ_{S1}, $|\lambda_{S1}|$, $|\lambda_{S2}|$ and M_2/M_1 as a function of the mass of ϕ_1. The color code represents the maximum energy scale where the point keeps the scalar potential positivity unbroken. The benchmark points in the plot are listed in the table 4.3.

(left) present the evolution, where the Higgs self-coupling breaks the vacuum stability at $10^{10.6}$ GeV $\lesssim \Lambda \lesssim 10^{10.9}$ GeV. However, we found points where the Higgs self-coupling decreases whilst the energy scale increases, but change their behavior at some energy scale, then do not broken the vacuum stability (figure 4.7−right panel).

The reason of the Higgs self-coupling behavior comes from its β-function,

Parameter	Point 1	Point 2	Point 3	Point 4	Point 5
λ_{41}	2.4798	0.0624	0.3423	0.0049	0.2273
λ_{42}	0.0006	0.3767	0.0007	0.0003	0.5123
λ_{S1}	0.0024	0.0001	0.2727	-0.0002	0.0046
λ_{S2}	0.0007	0.5896	2.6574	0.2191	-0.3834
M_1 (GeV)	58.12	705.55	1952.8	149.54	414.98
M_2 (GeV)	90.98	1117.92	1978.25	193.91	435.83
μ_{S1} (GeV)	206.64	7916.0	9795.41	2872.28	1968.29
$\Omega_1 h^2$	0.129	0.124	0.105	0.117	0.115
$\Omega_2 h^2$	2.57×10^{-5}	0.0045	0.0067	4.67×10^{-34}	0.0024
$\Omega_{\mathrm{DM}} h^2$	0.129	0.1285	0.1117	0.117	0.1174
Ω_1/Ω_2	5019.46	27.56	15.65	2.51×10^{32}	47.13
σ_1^{SI} (pb)	1.45×10^{-11}	2.10×10^{-16}	1.72×10^{-10}	1.46×10^{-14}	1.06×10^{-12}
σ_2^{SI} (pb)	4.61×10^{-13}	2.45×10^{-9}	1.59×10^{-8}	1.12×10^{-8}	6.79×10^{-9}
$\log(\Lambda_{\mathrm{max}}/\mathrm{GeV})$	17.0	17.0	17.0	17.0	12.8

Table 4.3: Benchmark points for scalar potential positivity, that fulfill the constraint up to some energy scale Λ_{max}. The table displays all the free parameters of the model at the top quark mass energy scale. All of them except point 5 are viable under this condition up to energies around the GUT scale.
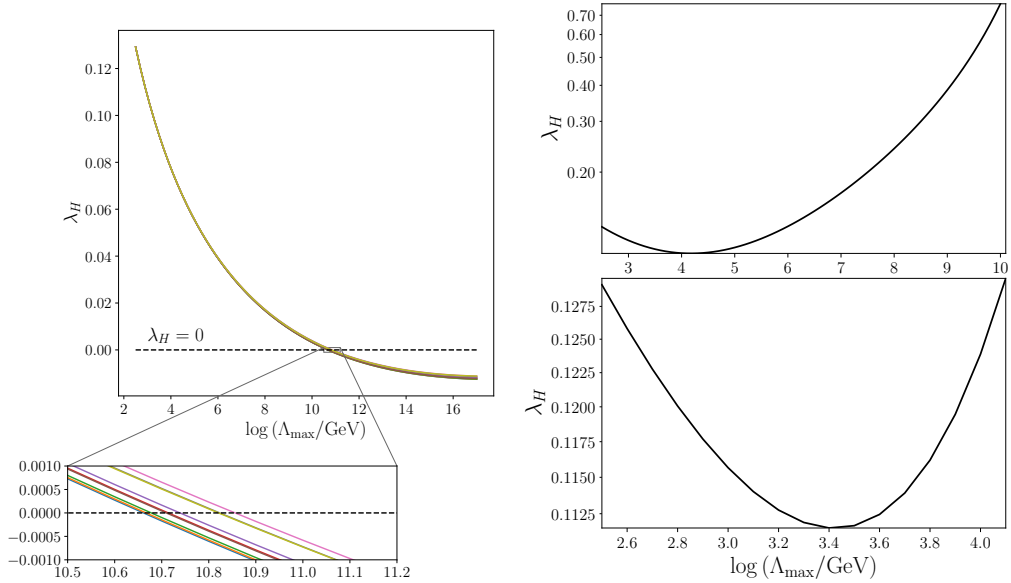

Figure 4.7: The behavior of λ_H as a function of the energy scale $\log(\Lambda_{\mathrm{max}}/\mathrm{GeV})$ after of running the RGEs. Left: eight benchmark points that break the vacuum stability taking negative values of the Higgs self-coupling. Right: two benchmark points characterized by its change of monotony in the Higgs self-coupling behavior along the energy scales.

which includes the terms

$$8\pi^2\beta_{\lambda_H}^{(2)} \supset (5\lambda_H - \lambda_{S1})\lambda_{S1}^2 + (5\lambda_H - \lambda_{S2})\lambda_{S2}^2. \tag{4.3}$$

Then we observe that when the Higgs coupling with DM particles increases with energy scale, the Higgs self-coupling decreases. However, it is not guaranteed for all the points, since it may happen that gauge and Yukawa coupling of top quark represent the largest contribution to λ_H. On the other hand, since this analysis has been carried out using the β-functions with two loops, the dependence on λ_{Si} of this function for the self-coupling of the Higgs is given precisely because it admits processes with two loops; when considering one-loop processes, there is no dependency on λ_{Si}, and therefore, the viability of the parameter space could change in terms of the stability of the vacuum.

To explore how the sign of the Higgs couplings influences the viability of the model, in figure 4.8 we plot the impact of λ_{41} and λ_{42} in the positivity condition. This shows that the region where $\lambda_{S1}, \lambda_{S2} > 0$ is viable. On the other hand, we may observe that an increase in DM self-coupling leads to changes in the zones of viability. The top-left of the figure starts with weak DM self-interactions but while they increase up to $\lambda_{4i} = 1$ (bottom-right), the model allows regions in the plane where $\lambda_{S1}\lambda_{S2} < 0$. Of course, energies of the order of 10^{16} GeV like those shown in the figure 4.8 are quite high, but they make it possible to see that the model fulfills the condition at considerable energy scales. However, it is interesting to observe the mentioned case $\lambda_{4i} = 1$ (bottom-right panel), where

negative values are allowed for only one of the couplings at scales up to 10^7 GeV. The four panels of the mentioned figure show that the case $\lambda_{S1}, \lambda_{S2} < 0$ is forbidden since it does not verify the conditions for positivity.
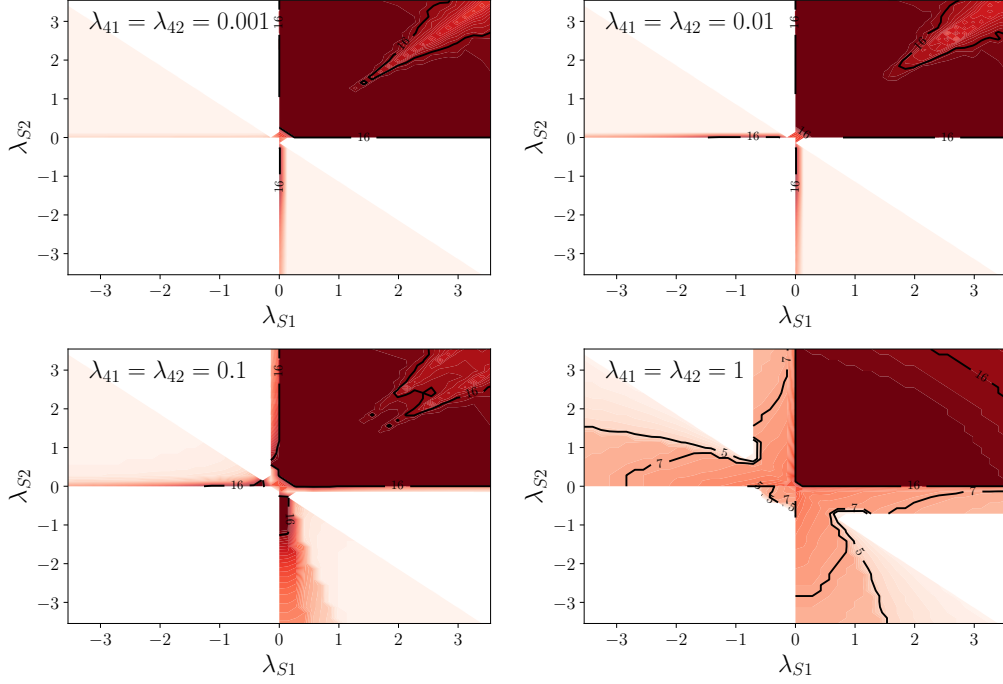

Figure 4.8: The allowed regions in the plane $(\lambda_{S2}, \lambda_{S1})$ which maintain the scalar potential positivity at different energy scales given fixed values of λ_{4i}. The color code describes the viability of the model relative to the value of $\log(\Lambda_{\max}/\text{GeV})$ which encloses the curves.

In addition, we want to study how is the impact of the couplings of one of the DM particles on the other. The figure 4.9 shows the plane $(\lambda_{S1}, \lambda_{41})$ fixing the values of λ_{42} and λ_{S2}, where in the bottom-left plot we observe viability to GUT energy scales due the negative value of Higgs coupling with ϕ_1. We observe that the parameters associated with one of the particles influence the admissible values of the second particle to verify a viable model under positivity. We note that the region $\lambda_{S1} > 0$ is viable at high energy scales for any value of λ_{S2} and
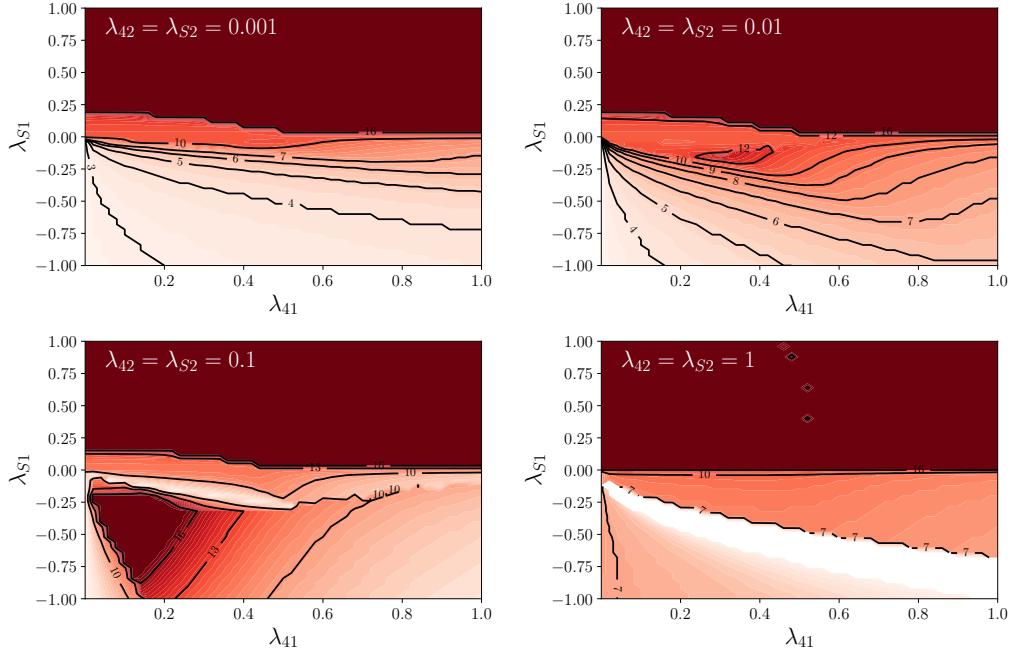
Figure 4.9: The allowed regions in the plane $(\lambda_{S1}, \lambda_{41})$ which maintain the scalar potential positivity at different energy scales given fixed values of λ_{42} and λ_{S2}. The color code describes the viability of the model relative to the value of $\log(\Lambda_{\max}/\text{GeV})$ which encloses the curves.

λ_{42}, but significant changes are observed in the regions of $\lambda_{S1} < 0$.

To examine in depth how the values of λ_{S2} influence λ_{S1} at very high energy scales, the figure 4.10 shows models with $\Lambda_{\max} \geq 10^{16}$ GeV, and implies the necessity of having one of the DM particles featuring a sizeable λ_{Si}. This restriction is significant in case of taking into account the feasibility of the model at these scales, however, for $\Lambda \sim 10^4$ GeV or up to $\Lambda \sim 10^7$ GeV, the plane $(\lambda_{S2}, \lambda_{S1})$ is not restricted considerably.

As a synthesis, we state that the positivity of the scalar potential has shown that the parameter space verifies viability at high energy scales, provided that $\lambda_{S1}, \lambda_{S2} > 0$ or $\lambda_{S1} \lambda_{S2} < 0$. The stability of the vacuum is not guaranteed for
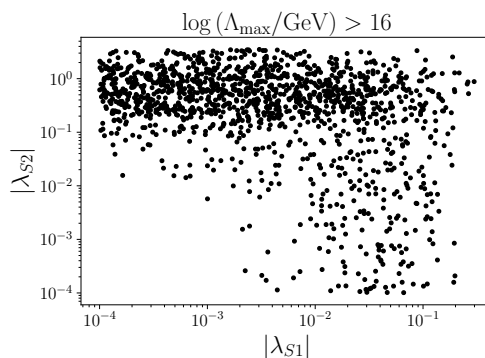
Figure 4.10: Viable values of Higgs coupling with ϕ_2 (λ_{S2}) as a function of its coupling with ϕ_1 (λ_{S1}). The figure displays the values at the top quark energy scale for both couplings, which guarantee the scalar potential positivity in the case $\lambda_{S1}\lambda_{S2} < 0$.

all points due to the dependence of the β-Higgs function on two loops. On the other hand, the benchmark points do not show recurring behavior precisely because of the viability of the general region initially considered. Finally, when considering energy scales of the GUT order, we can talk about restrictions that can be studied by works concerned with the viability of the model at said scales.

4.5 SCALAR POTENTIAL STABILITY

Ensuring the SM global minimum is a complex task in this model since we have a set of eight possible minima, according to (3.23). Since evaluating this condition involves the solution of the (3.24) equations, it has been solved numerically to evaluate the values of the minima of the fields over the scalar potential implemented in `Wolfram_Mathematica_13` . In this way, we developed a scan that satisfies the stability constraints (*see* figure 4.11). The majority of the points in the scan are blue, then the stability is broken to low energy scales;

however, there are points that survive to high energies. It is important to mention that these excluded regions that break the condition at low energy scales do verify it at the top quark mass scale, of course.
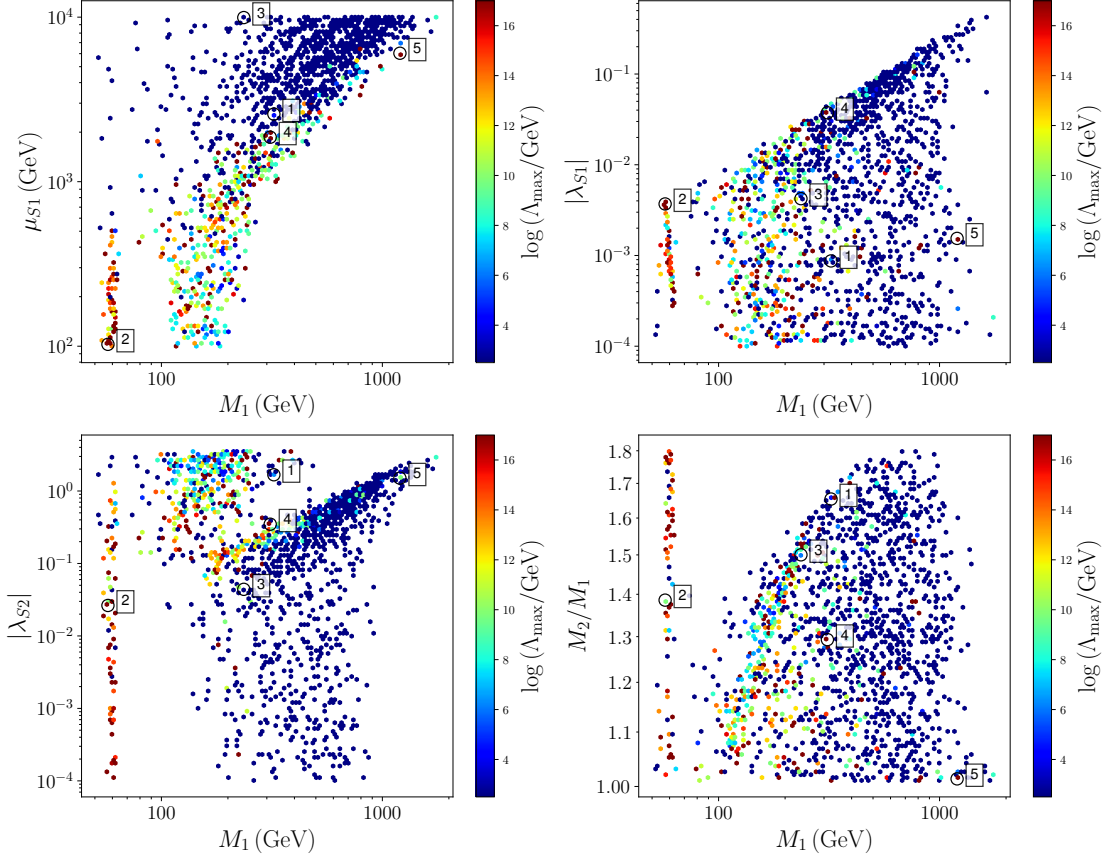

Figure 4.11: Viable parameter space with scalar potential stability at energy scales up to GUT. The figure shows the free parameters μ_{S1}, $|\lambda_{S1}|$, $|\lambda_{S2}|$ and M_2/M_1 as a function of the mass of ϕ_1. The color code represents the maximum energy scale where the point remains the SM minimum stable as global. The benchmark points in the plot are listed in the table 4.4.

Once again we choose a set of five benchmark points with different features: three of them are viable at GUT energy scales, and the other two break stability at $\Lambda_{\max} \sim 10^3$ and 10^6 GeV as shows the table 4.4. First, we observe that all the points except point 4, are such that $\lambda_{S1}\lambda_{S2} < 0$. This feature will play an important role in the combination of constraints since as we saw in the past

section, positivity leads to stringent bounds when this happens. On the other hand, *all* of the points do not pass the perturbative unitarity filter due to their λ_{4i} values (if we only take into account very large Λ); according to the discussion in the section 4.3, this breaks that condition at low energy scales and does not achieve perturbative unitarity at GUT energy scales.

Parameter	Point 1	Point 2	Point 3	Point 4	Point 5
λ_{41}	2.825	0.2523	1.4123	2.3072	2.7987
λ_{42}	2.5346	0.3937	0.0014	2.3547	1.9836
λ_{S1}	0.0009	-0.0037	-0.0042	0.0374	-0.0015
λ_{S2}	-1.6753	0.0263	0.044	0.3482	1.5053
M_1 (GeV)	322.8	57.28	235.93	310.8	1200.75
M_2 (GeV)	533.95	79.38	353.94	401.92	1216.81
μ_{S1} (GeV)	2576.0	102.66	9941.96	1863.13	6035.15
$\Omega_1 h^2$	0.11	0.119	0.119	0.126	0.106
$\Omega_2 h^2$	1.51×10^{-8}	0.0002	1.99×10^{-7}	0.0022	0.0044
$\Omega_{\mathrm{DM}} h^2$	0.11	0.1192	0.119	0.1282	0.1104
Ω_1/Ω_2	7.28×10^6	610.26	5.98×10^5	58.33	24.2
σ_1^{SI} (pb)	6.39×10^{-14}	3.56×10^{-11}	2.81×10^{-12}	1.27×10^{-10}	1.45×10^{-14}
σ_2^{SI} (pb)	8.65×10^{-8}	9.48×10^{-10}	1.35×10^{-10}	6.59×10^{-9}	1.35×10^{-8}
$\log(\Lambda_{\mathrm{max}}/\mathrm{GeV})$	6.3	17.0	2.6	17.0	17.0

Table 4.4: Benchmark points that ensure to maintain the SM minimum of the scalar potential as global. The showed points fulfill the constraint up to some energy scale Λ_{max}. The table displays all the free parameters of the model at the top quark mass energy scale, and points 2, 4, and 5 are viable under this condition at energies beyond GUT.

Since the (μ_{S1}, M_1) and $(|\lambda_{S1}|, M_1)$ planes present the most homogeneous regions with points with stability broken at low energy scales, we plot the same planes setting $\Lambda_{\mathrm{max}} > 10^4$ GeV in order to neglect this points and see better the exclusion zones for these parameters; we show this in figure 4.12. All the points which fulfill stability at GUT energy scales verify $M_1 \lesssim 1.2$ TeV which is the mass value of point 5. On the other hand, it is interesting to observe that the

$M_1 \sim 40$ GeV region has a wide interval for the values of the other parameters in which the condition is verified at high energy scales.

We see then that the figure 4.12 shows an important restriction in the planes, which prevails for high energy scales. Unlike the previously studied conditions, the stability of the scalar potential is highly restrictive if the model is expected to exceed scales of 10^4 GeV. Once again, the non-correlation found between the benchmark points is highlighted.
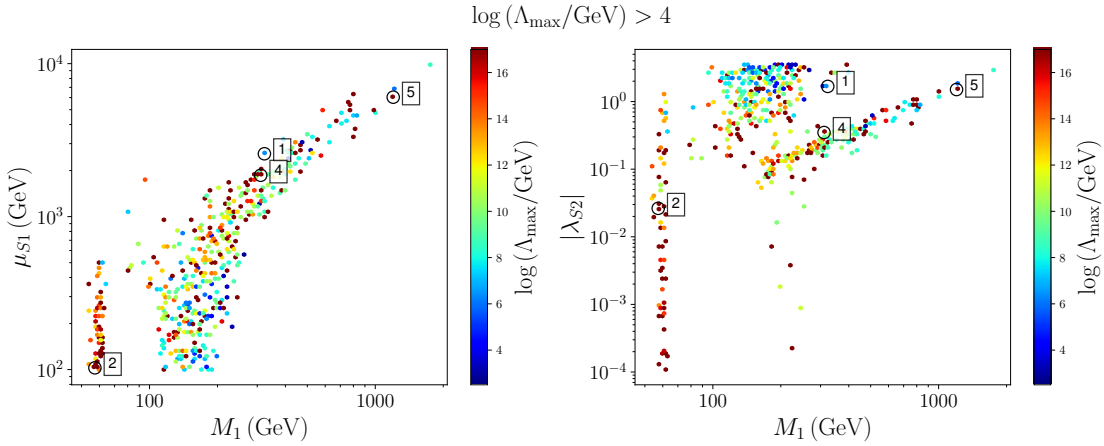

Figure 4.12: Viable parameter space with scalar potential stability at energy scales up to GUT. The figure shows the free parameters μ_{S1} and $|\lambda_{S2}|$ as a function of the mass of ϕ_1. The color code represents the maximum energy scale (from $\Lambda_{\mathrm{max}} > 10^4$ GeV) where the point remains the SM minimum stable as global.

4.6 COMBINATION OF CONSTRAINTS

In this section we study the impact of imposing *all* the theoretical bounds at once. Of course, we expect a wide restriction in each parameter, especially in Higgs couplings with DM and trilinear couplings such as we saw previously.
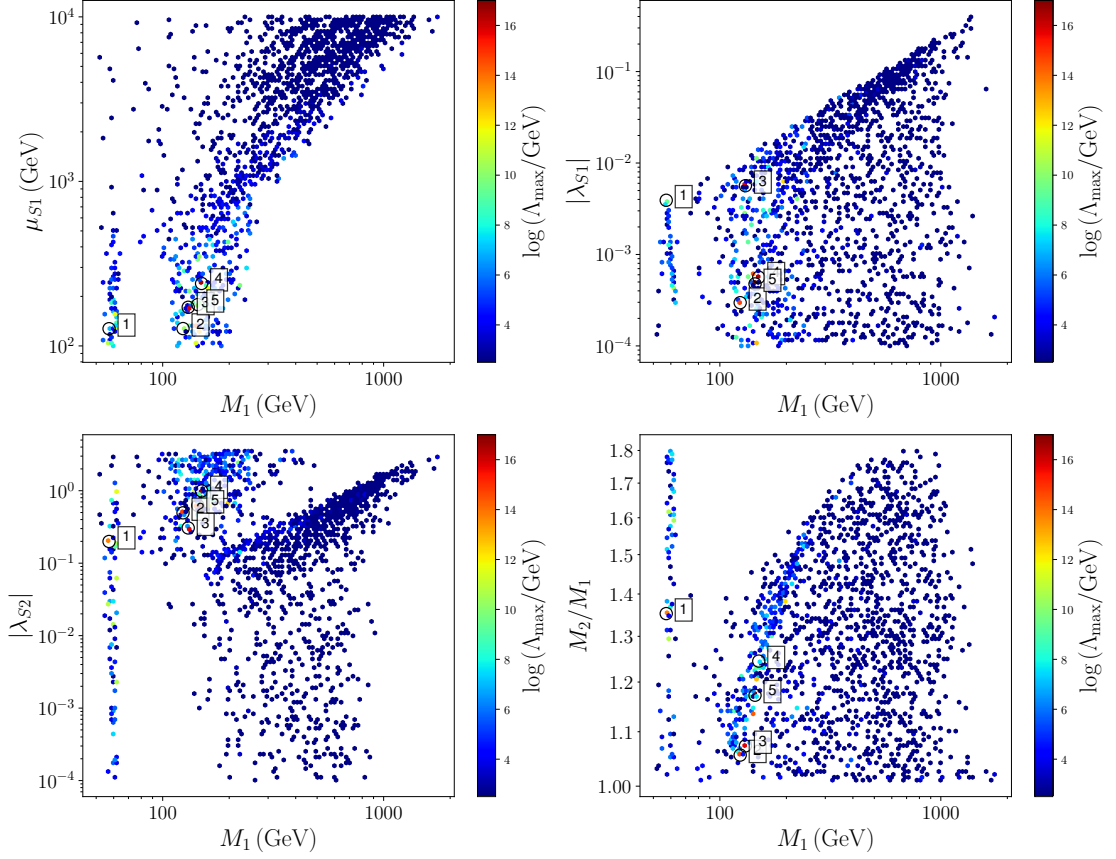
Figure 4.13: Viable parameter space with the theoretical bounds combined at energy scales up to GUT. The figure shows the free parameters $\mu_{S1}, |\lambda_{S1}|, |\lambda_{S2}|$ and M_2/M_1 as a function of the mass of ϕ_1. The color code represents the maximum energy scale where the point remains all of the conditions unbroken. The benchmark points in the plot are listed in the table 4.5.

On the other hand, we expect after combining the constraints further excluded regions arise due to the necessity of fulfilling each one, i.e., is not only a "superposition" of the previously observed constraints.

In order to combine the constraints, we selected points that verify all the restrictions at the top quark mass energy scale. Then we run the RGEs and determine the Λ_{max}-energy scale where any condition breaks, so that the model is viable up to that energy scale. We show the results in the figure 4.13. The benchmark points plotted in the figure are such that they fulfill the constraints

Parameter	Point 1	Point 2	Point 3	Point 4	Point 5
λ_{41}	0.3174	0.2931	0.2703	0.1756	0.186
λ_{42}	0.0925	0.0001	0.0004	0.0863	0.0003
λ_{S1}	0.0039	-0.0003	-0.0056	0.0006	-0.0005
λ_{S2}	0.1992	0.4952	0.3063	-0.9917	0.6255
M_1 (GeV)	57.18	123.58	130.48	149.96	144.22
M_2 (GeV)	77.35	130.5	140.01	186.67	169.11
μ_{S1} (GeV)	127.26	127.46	171.73	239.57	178.26
$\Omega_1 h^2$	0.117	0.117	0.127	0.123	0.12
$\Omega_2 h^2$	0.0001	2.57×10^{-7}	3.19×10^{-5}	8.31×10^{-13}	1.00×10^{-6}
$\Omega_{\mathrm{DM}} h^2$	0.1171	0.117	0.127	0.123	0.12
Ω_1/Ω_2	1539.47	4.55×10^5	3981.19	1.48×10^{11}	1.17×10^5
σ_1^{SI} (pb)	4.00×10^{-11}	5.03×10^{-14}	1.63×10^{-11}	1.23×10^{-13}	9.50×10^{-14}
σ_2^{SI} (pb)	5.71×10^{-8}	1.25×10^{-7}	4.16×10^{-8}	2.46×10^{-7}	1.19×10^{-7}
$\log(\Lambda_{\mathrm{max}}/\mathrm{GeV})$	13.7	14.7	15.7	16.5	17.0

Table 4.5: Benchmark points that fulfill all of the combined constraints up to some energy scale Λ_{max}, ordered from the minimum energy scale values to the maximum. The table displays all the free parameters of the model at the top quark mass energy scale, and point 5 under the constraints, is viable at energies beyond of GUT. These points have the maximum values of Λ_{max} obtained in the scan.

to higher energy scales, for instance, there is a point that has $\Lambda_{\mathrm{max}} > 10^{17}$ GeV (point 5).

To detail the analysis to all the parameters, we have considered the planes of each parameter against the value of the energy scale. This is shown in the figure 4.14. First, we may see that all the benchmark points have DM masses below $M_1 \lesssim 150$ GeV, being the point 4 highest. In addition, all the benchmark points except point 1 show that $\lambda_{S1}\lambda_{S2} < 0$. However, though is a recurrent behavior, it is not necessary. Respect to the values of $|\lambda_{S1}|$ and $|\lambda_{S2}|$, the benchmark points show that all of them have suppressed interactions between ϕ_1 with Higgs boson but sizeable interactions between ϕ_2 with Higgs boson, i.e., $|\lambda_{S1}| << |\lambda_{S2}|$.

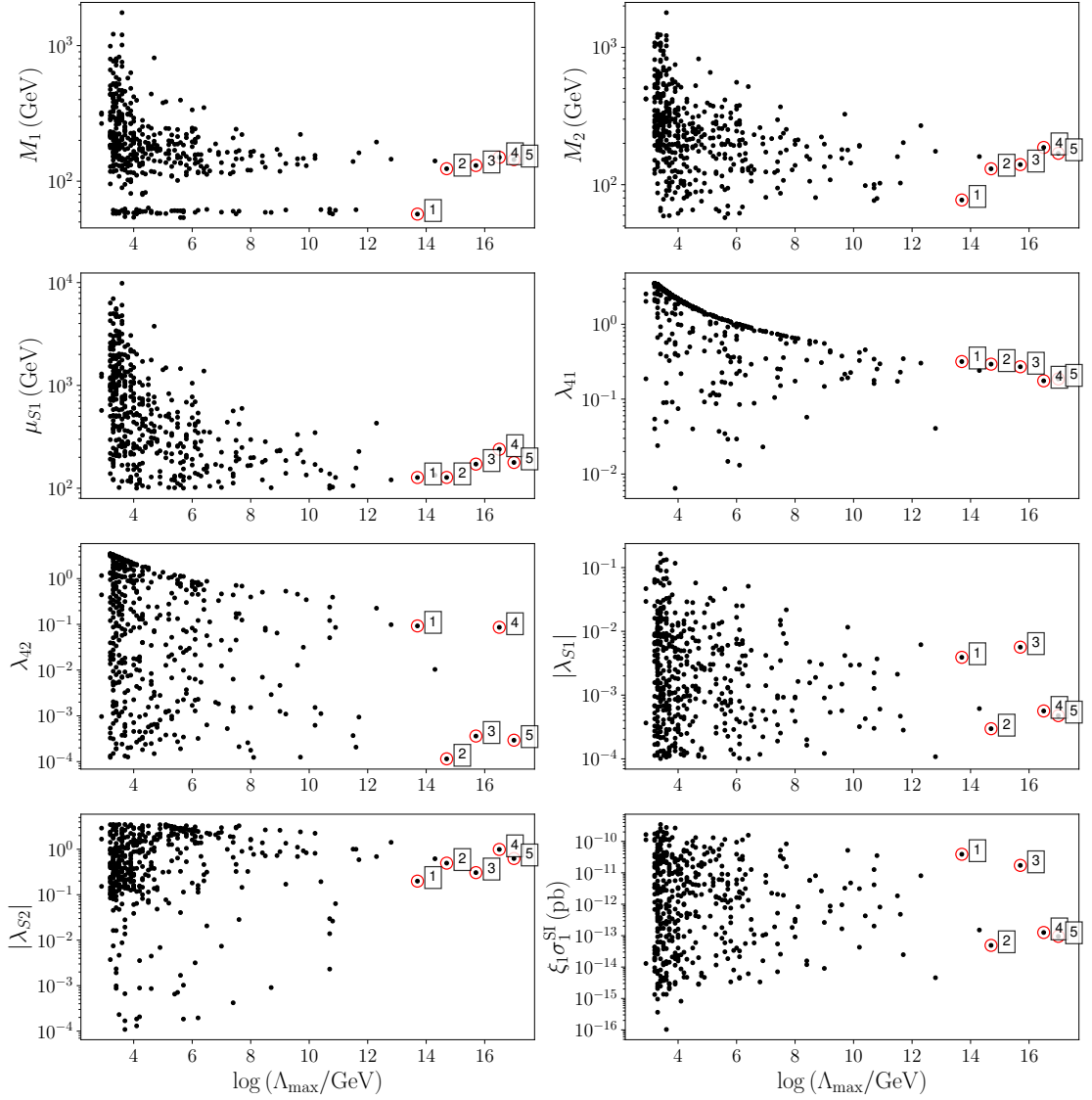In general, we emphasize the following observations to the parameter space

Figure 4.14: Evolution of the viable parameter space as a function of Λ. The figure displays the maximum value of the energy scale for a given point with specific values of each parameter where the model fulfills *all* of the constraints combined.

as a result of observing the planes in the figure 4.14.

- M_1 and M_2: The value of the mass should decrease when the model is expected to verify all conditions at high energy scales. The figures show how the mass takes smaller values as Λ_{max} increases.

60

- μ_{S1}: This trilinear coupling must also be restricted to lower values than those initially considered if a viable model is to be obtained at larger energy scales. For example, for benchmark points (where the energy is quite large), low values of this coupling correspond.

- λ_{41} and λ_{42}: The perturbative unitarity showed that these couplings have to decrease with the energy scale, as long as the model is expected to be viable at high scales. This behavior prevails in the current results. However, it can be seen that the decrease of λ_{41} is slightly faster than that of λ_{42}.

- λ_{S1} and λ_{S2}: The couplings between the DM particles and the Higgs behave differently. With respect to λ_{S1}, a behavior similar to that of the couplings λ_{4i} is observed, where the energy scale must be correlated with the decrease in the value of the coupling, that is, high energy scales imply imposing smaller values on the mass scale of the top quark than those initially considered. Additionally, it is observed that λ_{S1} at the energy scale of the top quark must take values below 0.2, while in principle $\sqrt{4\pi}$ was admitted as the maximum value. On the other hand, the coupling λ_{S2} presents a behavior opposite to that of λ_{S1}; it is observed that the high energy scale restricts the range of this parameter below. For example, for the benchmark points, the values are close to unity. Then, lower values are excluded as the viability scale increases.

- $\xi_1 \sigma_1^{\text{SI}}$: The values of the spin-independent cross section for elastic scattering with nuclei do not present a specific behavior at high scales of model

viability.

Although global restrictions are not obtained, but are clearly dependent on the energy scale for which viability is requested, it should be noted that there is a correlation between the implemented restrictions and the values admitted by the model parameters. The figures discussed allow us to observe the aforementioned, each plane presents a specific behavior with the energy scale.

The condition of keeping the parameter space real mainly influenced the values of λ_{S2} (*see* fig. 4.3). Perturbative unitarity has imposed important behaviors for the values of DM self-couplings with respect to the feasibility scale (*see* fig. 4.5). Scalar potential positivity constrains the values of the DM couplings with the Higgs, correlating these λ_{Si} with each other and with the self-couplings (*see* fig. 4.8, 4.9 and 4.10), also prohibiting points where $\lambda_{S1}, \lambda_{S1} < 0$; furthermore, vacuum stability is not guaranteed for all points due to the dependence of the Higgs self-coupling on λ_{Si} (*see* fig. 4.7). The stability of the scalar potential, by guaranteeing the minimum of the SM as global, eliminates many points that verify the condition at the energy scale of the top quark mass and reduces the admitted values for all parameters (*see* fig 4.11 and 4.12).

4.7 CONSTRAINTS WITH $\lambda_{412}, \lambda_{3i}, \mu_{S2} \neq 0$

When considering the new coupling parameters associated with the DM conversion ($\lambda_{412}, \lambda_{3i}$) and the trilinear term for semi-annihilations of ϕ_2, the model

acquires a greater number of combinations for the parameter space, and the behaviors at high energy scales change, allowing different regions in the studied planes that with $\lambda_{412} = \lambda_{3i} = \mu_{S2} = 0$ were prohibited. On the other hand, the β-functions associated with these new parameters can also become unstable and acquire complex values at certain energy scales. The figures 4.15 and 4.16, show some results obtained from the scan when the mentioned parameters are considered. It is observed that the perturbative unitarity similarly constrains the quartic couplings λ_{3i}. The combination of the constraints eliminates many viable points, such that the maximum energy scale obtained in the scan is around 10^7 GeV, which is important since the viability of the model is demonstrated at high scales of energy, even with all the parameters taking non-zero values. Finally, the change in the constraints of μ_{S1} and the DM masses when considering these additional parameters is highlighted; we note that larger values are allowed according to the increment of the energy scale compared to the figure 4.14.
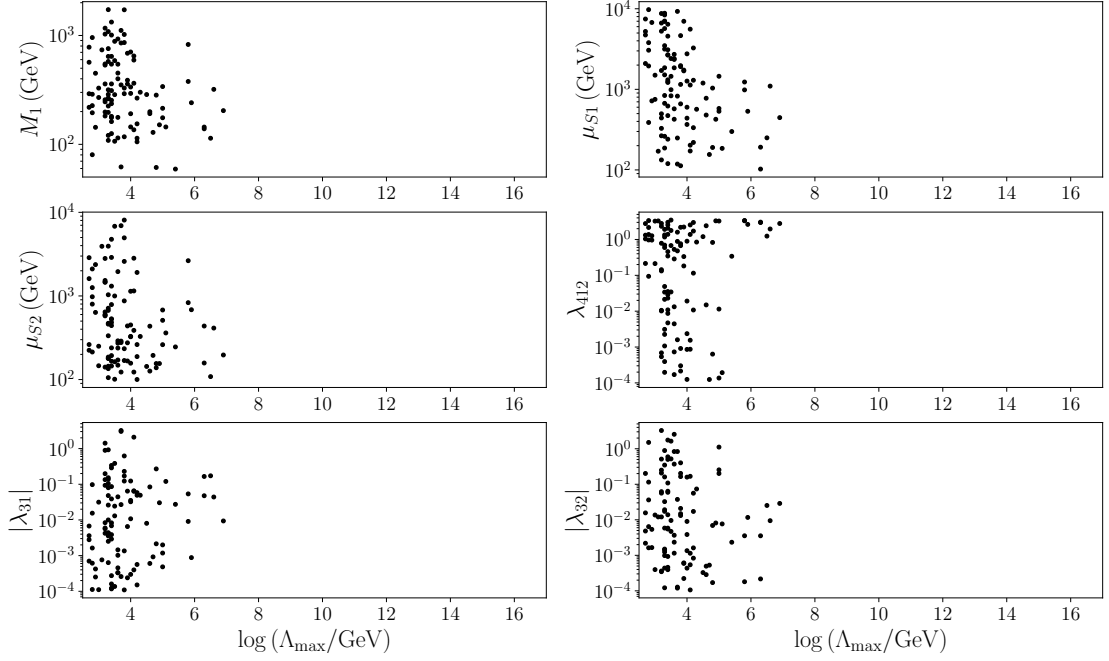
Figure 4.15: The combination of constraints over the parameter space, taking $\lambda_{412}, \lambda_{3i}, \mu_{S2} \neq 0$. The figure plots the energy scale where each parameter breaks the considered constraints.
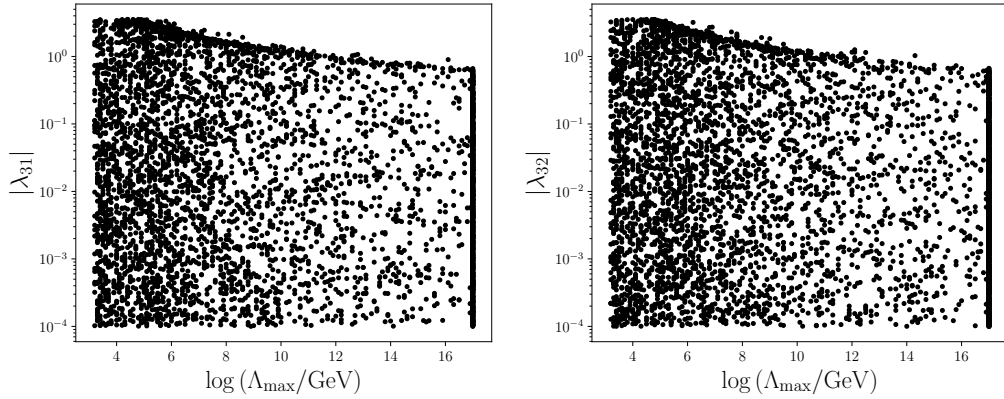

Figure 4.16: Evolution of the viable λ_{31} and λ_{32} as a function of Λ. The figure displays the maximum value of the energy scale for a given point with specific values of these parameters where the model fulfills the perturbative unitarity bound.

5

Discussion and conclusions

We have studied the $\mathbb{Z}_5$ model of two-component DM. Initially, we consider the admitted values for the free parameters, taking into account the phenomenology reported in [43]. With this, we did a scan over the parameter space to guarantee that the points under study, verify the constraints of relic density and direct detection. After having a large set of points that verify these conditions, we evaluate new theoretical constraints at energy scales in the range $10^{5/2} \leq \Lambda_{\mathrm{max}}/\mathrm{GeV} \leq 10^{17}$, with the purpose of exploring how perturbative unitarity, positivity and stability of the scalar potential impose new limits on the free parameters of the model over these energy scales. This type of analysis has suggested important constraints and behaviors of the parameter space:

- *Keep parameter space values real*: Viability at high energy scales, greater than $\Lambda \sim 10^8$ GeV, can lead the λ_{S2} coupling to take complex values over a wide range of values considered at the top quark mass scale.

- *Perturbative unitarity*: Keeping the S-matrix unitary implies reducing the maximum value that the self-couplings λ_{4i}, the coupling λ_{S2} and the quartic couplings λ_{3i} can take. It was observed that increasing the energy scale up to which the model maintains perturbative unitarity restricts the admitted value for these couplings to the top quark mass scale.

- *Scalar potential positivity*: Although phenomenologically there are points that verify the restrictions of direct detection experiments and the relic density condition, this condition showed that if these points are such that $\lambda_{S1}, \lambda_{S2} < 0$, the matrix of couplings does not hold copositive, and therefore, the positivity of the scalar potential does not hold. In addition, the viability of points with $\lambda_{S1}\lambda_{S2} < 0$ was checked, restricted to the values taken by the DM self-couplings and the expected viability energy scale. The stability of the vacuum is not guaranteed for all points, since some points break it at $\Lambda \sim 10^{10}$ GeV due to the behavior of Higgs self-coupling dependent on the λ_{Si} couplings.

- *Scalar potential stability*: Imposing the globality of the minimum of the scalar potential as the minimum of the SM ($\not\!\!\!EW, \mathbb{Z}_5$) greatly restricts the values that the DM masses can take, the new trilinear couplings μ_{Si} and even the couplings of the DM with the Higgs λ_{Si}, so that the energy scale up to which the model verifies this condition influences the value that these parameters can acquire. High energy scales imply values smaller than the mass scale of the top quark.

These remarks apply for values of $\lambda_{412}, \lambda_{3i}, \mu_{S2}$ zero and non-zero. However, for the non-zero case, the maximum energy scale obtained is highlighted: 10^8 GeV.

The $\mathbb{Z}_5$ model is the minimum $\mathbb{Z}_N$ model that allows a multi-component DM scenario with two *complex* fields. The results obtained in this research can be extended to models for $N > 5$. For instance, the scalar potential of the model $\mathbb{Z}_7$ allowing for three complex fields, in general, contains the interaction terms

$$\mathcal{V}_3 \supset \phi_2^2\phi_3, \phi\phi_3^2, \phi_1^2\phi_2^*, \phi_1\phi_2\phi_3^*, \tag{5.1}$$

$$\mathcal{V}_4 \supset \phi_1\phi_2^3, \phi_1^2\phi_2\phi_3, \phi_2\phi_3^2\phi_1^*, \phi_1^2\phi_1^{*2}, \phi_3\phi_1^{*3}, \phi_3^3\phi_2^*, \phi_1\phi_2\phi_1^*\phi_2^*, \phi_2^2\phi_2^{*2}, \phi_1\phi_3\phi_2^{*2},$$

$$\phi_1\phi_3\phi_1^*\phi_3^*, \phi_2\phi_3\phi_2^*\phi_3^*, \phi_3^2\phi_3^{*2}, \tag{5.2}$$

$$\mathcal{V}_5 \supset \phi_1^4\phi_3, \phi_2\phi_3^4, \phi_1\phi_2^{*4}, \tag{5.3}$$

to which correspond more free parameters than those studied in this research. Of course, this number of parameters leads to complicated conditions, but they are largely satisfied by the large number of combinations that can be generated with the parameter values. We can state that the results associated with this type of model must be similar to those obtained with the $\mathbb{Z}_5$ model, where most of the regions of the parameter space fulfill the viability at several energy scales.

The $\mathbb{Z}_5$ model is considered as a prototype for other two-component DM models. A key piece of this model is the trilinear coupling μ_{S1}. Other models such as $\mathbb{Z}_9$ (four complex fields), also allow trilinear terms associated with DM

semi-annihilations such as $\mu_{S2}\phi_2^2\phi_4^*$. The $\mathbb{Z}_{10}$ model (four complex fields and one real field) has a Lagrangian similar to the $\mathbb{Z}_5$, which allows trilinear (μ_{Si}) and quartic terms (λ_{3i}). The results can be extended to these models analogous to $\mathbb{Z}_5$.

Although this type of analysis is not recurrent in the literature, research such as [44], like this research, have found limits on the $\mathbb{Z}_N$ models for $N \leq 3$. Future works in this field can examine the viability of these models under the considerations presented here. Also, one can think of applying the theory presented to possible extensions of the $\mathbb{Z}_5$ model. For example, the simplest extension consists in associating the symmetry $\mathbb{Z}_5$ to a spontaneously broken gauge symmetry $U(1)_X$. Thus, the trilinear term μ_{S1} is allowed, but μ_{S2} requires a new vacuum expectation value. The model can also be extended as scotogenic, considering extra fields that explain the neutrino masses through vectorlike fermions, Majorana masses for neutrinos (at two-loops) can be generated. For an exposition of this topic in detail, see [43, 50–52].

Acknowledgments

References

[1] E. Hubble and M. L. Humason, "The Velocity-Distance Relation among Extra-Galactic Nebulae," APJ **74**, 43 (1931)

[2] J. H. Oort, "The force exerted by the stellar system in the direction perpendicular to the galactic plane and some related problems," Bull. Astron. Inst. Netherlands **6**, 249–287 (1932)

[3] F. Zwicky, "Republication of: The redshift of extragalactic nebulae," General Relativity and Gravitation **41**, 207–224 (2009)

[4] F. Zwicky, "On the Masses of Nebulae and of Clusters of Nebulae," APJ **86**, 217 (1937)

[5] J. F. Meekins *et al.*, "Physical Sciences: X-rays from the Coma Cluster of Galaxies," Narute **231**, 107–108 (1971)

[6] P.J. Peebles, "Large-scale background temperature and mass fluctuations due to scale-invariant primeval perturbations," APJL **263**, L1–L5 (1982)

[7] D. Walsh, R. F. Carswell, and R. J. Weymann, "0957+561 A, B: Twin quasistellar objects or gravitational lens?." Nature **279**, 381–384 (1979)

[8] A. D. Chernin, "The Rest Mass of Primordial Neutrinos and Gravitational Instability in the Hot Universe," Soviet Astronomy **25**, 14–16 (1981)

[9] A. A. Penzias and R. W. Wilson, "A Measurement of Excess Antenna Temperature at 4080 Mc/s.." APJ **142**, 419–421 (1965)

[10] N. Aghanim *et al.*, "Planck 2018 results: Vi cosmological parameters," AAP **641**, A6 (2020), arXiv:1807.06209 [astro-ph.IM]

[11] G.C. Branco *et al.*, "Theory and phenomenology of two-higgs-doublet models," Physics Reports **516**, 1–102 (2012), arXiv:1106.0034 [hep-ph]

[12] E. Morgante, "Simplified dark matter models," AHEP **2018**, 1 (2018), arXiv:1804.01245 [hep-ph]

[13] J. Magaña and T. Matos, "A brief review of the scalar field dark matter model," JPCS **378**, 012012 (2012), arXiv:1201.6107 [astro-ph.CO]

[14] K. Garrett and G. Duda, "Dark matter: A primer," Adv. in Astron. **2011**, 1–22 (2011), arXiv:1006.2483 [hep-ph]

[15] G. Bertone and D. Hopper, "History of dark matter," Reviews of Modern Physics **90**, 1 (2018), arXiv:1605.04909 [astro-ph.CO]

[16] V. C. Rubin, W. Ford, and Jr. Kent, "Rotation of the Andromeda Nebula from a Spectroscopic Survey of Emission Regions," APJ **159**, 379 (Feb. 1970)

[17] A. Einstein, "Lens-like action of a star by the deviation of light in the gravitational field," Science **84**, 506–507 (1936)

[18] L. Sidney, "Gravitational lenses," Phys. Rev. **133**, B835–B844 (1964)

[19] E. W. Kolb and M. S. Turner, *The Early Universe*, Vol. 69 (1990) ISBN 978-0-201-62674-2

[20] R. H. Alex, G. Evan, and C. A. Fred, "Nuclear processes in other universes: Varying the strength of the weak force," Physical Review D **98**, 1 (2018), arXiv:1809.05128 [astro-ph.CO]

[21] C. Smoot *et al.*, "Cobe differential microwave radiometers - instrument design and implementation," TAJ **360**, 685–695 (1990)

[22] N. Jarosik *et al.*, "Seven-year wilkinson microwave anisotropy probe (wmap) observations: Sky maps, systematic errors, and basic results," TAJSS **192**, 14 (2011), arXiv:1001.4744 [astro-ph.CO]

[23] G. Jungman, M. Kamionkowski, and K. Griest, "Supersymmetric dark matter," Physics Reports **267**, 195–373 (1996), arXiv:hep-ph/9506380 [hep-ph]

[24] L. Bergström, "Non-baryonic dark matter: observational evidence and detection methods," RPP **63**, 793–841 (2000), arXiv:hep-ph/0002126 [hep-ph]

[25] P. Gondolo, "Cosmic abundances of stable particles: Improved analysis," Nuclear Physics B **360**, 145–179 (1991)

[26] L. Goodenough and D. Hooper, "Possible evidence for dark matter annihilation in the inner milky way from the fermi gamma ray space telescope," JHEP, 1(2009), arXiv:0910.2998 [hep-ph]

[27] P. Gondolo and J. Silk, "Dark matter annihilation at the galactic center," Phys. Rev. Lett. **83**, 1719–1722 (1999), arXiv:astro-ph/9906391 [astro-ph]

[28] G. Steigman and M. S. Turner, "Cosmological constraints on the properties of weakly interacting massive particles," Nuclear Physics B **253**, 375–386 (1985)

[29] Akerib *et al.* D.S. (LUX-ZEPLIN Collaboration), "Projected wimp sensitivity of the lux-zeplin dark matter experiment," Phys. Rev. D **101**, 052002 (2020), arXiv:1802.06039 [astro-ph.IM]

[30] Y. Meng *et al.* (PandaX-4T Collaboration), "Dark matter search results from the pandax-4t commissioning run," Phys. Rev. Lett. **127**, 1 (2021), arXiv:2107.13438 [hep-ex]

[31] E. Aprile *et al.* (XENON Collaboration 7), "Dark matter search results from a one ton-year exposure of xenon1t," Phys. Rev. Lett. **121**, 111302 (2018), arXiv:1805.12562 [astro-ph]

[32] S. Chatrchyan, *et al.*, "Observation of a new boson at a mass of 125 gev with the cms experiment at the lhc," Physics Letters B **716**, 30–61 (2012), arXiv:1207.7235 [hep-ex]

[33] "Observation of a new particle in the search for the standard model higgs boson with the atlas detector at the lhc," Physics Letters B **716**, 1–29 (2012), arXiv:1207.7214 [hep-ex]

[34] W. Guo and Y. Wu, "The real singlet scalar dark matter model," JHEP, 1(2010), arXiv:1006.2518 [hep-ph]

[35] P. Athron *et al.*, "Status of the scalar singlet dark matter model," The European Physical Journal C **77**, 21 (05 2017), arXiv:1705.07931 [hep-ph]

[36] D.H. Weinberg *et al.*, "Cold dark matter: Controversies on small scales," PNAS-USA **112**, 20–57 (2013), arXiv:1306.0913 [hep-ph]

[37] G. Bélanger *et al.*, "Minimal semi-annihilating $\mathbb{Z}_n$ scalar dark matter," JCAP **2014**, 021–021 (2014), arXiv:1403.4960 [hep-ph]

[38] F. D'Eramo and J. Thaler, "Semi-annihilation of dark matter," JHEP **2010**, 20–57 (2010), arXiv:1003.5912 [hep-ph]

[39] G. Bélanger *et al.*, "Impact of semi-annihilations on dark matter phenomenology. an example of $\mathbb{Z}_n$ symmetric scalar dark matter," JCAP **2012**, 010–010 (2012), arXiv:1202.2962 [hep-ph]

[40] K. Agashe *et al.*, "Distinguishing dark matter stabilization symmetries using multiple kinematic edges and cusps," Physical Review D **82**, 434–501 (2010), arXiv:1003.0899 [hep-ph]

[41] M. De Montigny and M. Masip, "Discrete gauge symmetries in supersymmetric grand unified models," Phys. Rev. D **49**, 3734–3740 (1994), arXiv:hep-ph/9309312 [hep-ph]

[42] C. Yaguna and O. Zapata, "Multi-component scalar dark matter from a $\mathbb{Z}_n$ symmetry: a systematic analysis," JHEP **2020**, 48–110 (2020), arXiv:1911.05515 [hep-ph]

[43] G. Bélanger *et al.*, "The $\mathbb{Z}_5$ model of two-component dark matter," JHEP **2020**, 21–75 (2020), arXiv:2006.14922 [hep-ph]

[44] (2019), doi:\bibinfo{doi}{10.1007/jhep03(2019)204}

[45] K. Kannike, "Vacuum stability of a general scalar potential of a few fields," TEPJC **76**, 5–33 (2016), arXiv:1603.02680 [hep-ph]

[46] K. Kannike, "Vacuum stability conditions from copositivity criteria," TEPJC **72**, 11–31 (2012), arXiv:1205.3781 [hep-ph]

[47] S. Kanemura, T. Kubota, and E. Takasugi, "Lee-quigg-thacker bounds for higgs boson masses in a two-doublet model," Physics Letters B **313**, 155–160 (1993), arXiv:9303263 [hep-ph]

[48] (2018), doi:\bibinfo{doi}{10.1140/epjc/s10052-018-6127-z}

[49] J. Aalbers *et al.*, "DARWIN: towards the ultimate dark matter detector," JCAP **2016**, 017 (2016), arXiv:1606.07001 [astro-ph.IM]

[50] S. Ho, T. Toma, and K. Tsumura, "A radiative neutrino mass model with simp dark matter," JHEP **2017**, 110–135 (jul 2017)

[51] (may 2016), doi:\bibinfo{doi}{10.1007/jhep05(2016)030}

[52] M. Aoki and T. Toma, "Impact of semi-annihilation of $\mathbb{Z}_3$ symmetric dark matter with radiative neutrino masses," JCAP **2014**, 016–016 (sep 2014), arXiv:1405.5870 [hep-ph]